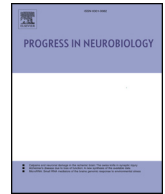




ELSEVIER

Contents lists available at ScienceDirect

Progress in Neurobiology

journal homepage: www.elsevier.com/locate/pneurobio

Original Research Article

3D cellular reconstruction of cortical glia and parenchymal morphometric analysis from Serial Block-Face Electron Microscopy of juvenile rat

Corrado Cali^{a,*}, Marco Agus^{b,c}, Kalpana Kare^a, Daniya J. Boges^a, Heikki Lehväslaiho^{a,d}, Markus Hadwiger^b, Pierre J. Magistretti^a^a BESE Division, KAUST, Thuwal, Saudi Arabia^b Visual Computing Center, KAUST, Thuwal, Saudi Arabia^c Visual Computing, CRS4, Pula, Italy^d CSC - IT Center for Science Ltd., Espoo, Finland

ARTICLE INFO

Keywords:

Astrocyte
Pericyte
Microglia
Neuron
3D reconstruction
3DEM

ABSTRACT

With the rapid evolution in the automation of serial electron microscopy in life sciences, the acquisition of terabyte-sized datasets is becoming increasingly common. High resolution serial block-face imaging (SBEM) of biological tissues offers the opportunity to segment and reconstruct nanoscale structures to reveal spatial features previously inaccessible with simple, single section, two-dimensional images. In particular, we focussed here on glial cells, whose reconstruction efforts in literature are still limited, compared to neurons. We imaged a 750,000 cubic micron volume of the somatosensory cortex from a juvenile P14 rat, with 20 nm accuracy. We recognized a total of 186 cells using their nuclei, and classified them as neuronal or glial based on features of the soma and the processes. We reconstructed for the first time 4 almost complete astrocytes and neurons, 4 complete microglia and 4 complete pericytes, including their intracellular mitochondria, 186 nuclei and 213 myelinated axons. We then performed quantitative analysis on the three-dimensional models. Out of the data that we generated, we observed that neurons have larger nuclei, which correlated with their lesser density, and that astrocytes and pericytes have a higher surface to volume ratio, compared to other cell types. All reconstructed morphologies represent an important resource for computational neuroscientists, as morphological quantitative information can be inferred, to tune simulations that take into account the spatial compartmentalization of the different cell types.

1. Introduction

Automated serial-section electron microscopy (3DEM), image stack processing, segmentation and 3D reconstructions are techniques that improved substantially in the last ten years, mostly driven by connectomics; however, its ambitious aim to image an entire human brain using electron microscopy to reconstruct every single synaptic connection is still for a distant future, although, very recently, an important milestone has been reached by imaging the entire brain of the drosophila (Zheng et al., 2018).

In contrast to connectomics that requires dense reconstructions to infer total connectivity of brain networks in mammals, several recent studies have taken advantage of similar imaging and reconstruction pipelines in order to study the ultrastructure of individual cells, a task achievable through the use of sparse reconstructions and focusing the analysis on neurons (Della Santina et al., 2016; Graydon et al., 2018;

Kasthuri et al., 2015; Morgan et al., 2016). A recent report investigated the different patterns of myelination in neocortical pyramidal neurons of mice from different cortical layers (Tomassy et al., 2014). Interestingly, the myelination profiles of individual reconstructed axons correlated with the size of the soma of the corresponding neuron, showing how different features might be extracted and quantified from 3D models.

The resolution of electron microscopy, together with the ease of large imaged volumes, also helped to investigate the intracellular organization of neuronal organelles at the whole cell level, in contrast to earlier works, limited by conventional serial section TEM (ssTEM), therefore focusing on the ultrastructure of individual structures, such as dendritic spines. For instance, (Bourne and Harris, 2011) highlighted the location of polyribosomes in enlarged, potentiated spines on 3D reconstructions. In the pioneering work from Lichmann's lab (Kasthuri et al., 2015) examples of reconstructed mitochondria, as well as

* Corresponding author.

E-mail address: corrado.cali@gmail.com (C. Cali).<https://doi.org/10.1016/j.pneurobio.2019.101696>

Received 20 January 2019; Received in revised form 12 September 2019; Accepted 17 September 2019

Available online 21 September 2019

0301-0082/ © 2019 The Authors. Published by Elsevier Ltd. This is an open access article under the CC BY license (<http://creativecommons.org/licenses/by/4.0/>).

synaptic vesicles from a reconstructed volume of $1500\ \mu\text{m}^3$ are shown; and in a report from De Camilli's lab, the authors explored the intimate relationship between mitochondria and endoplasmic reticulum (Wu et al., 2017). A recent work from the team of Graham Knott have produced an extensive collection of data from densely reconstructed blocks from layer I somatosensory cortex (Cali et al., 2018), including quantifications of volumes and surface areas of mitochondria. Although 3DEM cannot be considered as a high-throughput technique, it can be used to address morphological modifications following pathological impairments. A very recent report (Abdollahzadeh et al., 2019) describes how white matter axons and their ultrastructure including individual mitochondria, is impaired in rats following lesions; another work has used the same technique to analyze the ultrastructure of *Corpora amylacea* in human samples from aged or PD patients (Navarro et al., 2018). 3DEM pipeline is also a powerful tool to analyze non-brain samples; for instance, whole cultured cells and their intracellular ER and mitochondria were reconstructed to analyze their dynamics during cell division in a very elegant report (Puhka et al., 2012). Another work has addressed an in-depth 3D analysis of the African sleeping sickness parasite *Trypanosoma brucei* (Hughes et al., 2017) and its detailed intracellular organelles distribution.

The vast majority of 3D neuroanatomical studies based on 3DEM are focusing on neurons, with only a few examples of reconstructions and analysis of astrocytes or other non-neuronal cell types, as well as their intracellular content (Cali, 2017; Cali et al., 2016; Mohammed et al., 2017). In one report from the Ellismann group (Hama et al., 2004), entire astrocytes were rendered in 3D for the first time, and interesting quantifications such as surface area to volume ratio, or total perimeter were produced, even though images were not generated from serial sections, but from electron tomography. A later report focusing on the perivascular apposition of astrocytes, pericytes and endothelium (Mathiisen et al., 2010) showed nice 3D reconstructions of mitochondrial arrangements within astrocytes, generated from serial section electron micrographs.

Here, we combine the reconstruction of entire cells together with their intracellular content by imaging a volume of brain parenchyma from layer VI somatosensory cortex of a P14 rat, using a serial block-face scanning electron microscope (SBEM) equipped with a 3View module (Coggan et al., 2018). We identified several cell types within the imaged volume: neurons, astrocytes, microglia, pericytes, endothelial cells, and a few non-identifiable cells, most likely oligodendrocytes or precursors. We reconstructed four astrocytes, microglia, pericytes and four neurons. Although the imaged block was still too small to host the complete morphology of astrocytes and neurons, the reconstructed volume still contained all the proximal processes of these cells, showing for the first time in three-dimension the complexity of the astrocytic arborization. Also, we reconstructed the three-dimensional ultrastructure of microglial cells and pericytes in unprecedented detail, showed the location of their mitochondria, and provided empirical rules on how to distinguish each cell type on a single section micrograph.

2. Material and methods

2.1. Sample preparation

2.1.1. Rat fixation

Brain sections were a gift from Paola Bezzi (University of Lausanne, Switzerland). P14 rats were euthanized according to the Swiss Laws for the protection of animals. Animals were hosted in the animal facility of the Department of Fundamental Neuroscience (DNF) of the University of Lausanne, and did not show any sign of distress. 14 days old rat was deeply anesthetized with an i.p. injection of 150 mg/kg sodium-pentobarbital and killed by transcardially perfused fixative (2% PFA, EMS, 2.5% GA, EMS in PB 0.1 M 200 ml). 2 h after perfusion, brain was removed, and 100 μm coronal slices were cut using a Leica VT1000

vibratome. Sections were then collected and in PB 0.1 M and stored until embedding. We then selected sections including somatosensory cortex to proceed for staining and embedding in durcupan.

2.1.2. Staining for 3View

This protocol (Deerinck et al., 2010) was designed to enhance signal for backscatter electron imaging of resin-embedded mammalian tissue at low accelerating voltages (1–3 keV). The contrast of membranes is emphasized by using heavy metals incubation steps, as well as *en bloc* lead aspartate staining. 100 μm thick sections were washed into cacodylate buffer (0.1 M, pH7.4) prior postfixation for 1 h in ice-cold reduced osmium (1.5% KFeCN, 2% osmium tetroxide in 0.1 M cacodylate buffer). Sections were then rinsed in ddH₂O and placed in a freshly prepared, filtered thicarbonylhydrazide solution (1% TCH, Ted Pella in ddH₂O) at room temperature.

After 20 min, sections were washed in ddH₂O at room temperature and placed in a 2% osmium tetroxide solution in ddH₂O for 30 min. Following this second exposure to osmium, tissues were rinsed again and then placed in 1% uranyl acetate (aqueous) and left overnight at 4°. The next day, *en bloc* Walton's lead aspartate staining was performed: Sections were rinsed with ddH₂O at rising temperature (up to 60°), then immersed into warm (60°) lead aspartate solution (10 ml H₂O 0.04 g aspartic acid, 0.066 g lead nitrate. pH at 5.5 at 60°) for 20 min, inside an oven to assure that the temperature is kept constant during the incubation. Then sections were washed again in ddH₂O at room temperature, prior embedding in durcupan resin.

2.1.3. Embedding in durcupan

After heavy membrane staining, tissues were embedded in Durcupan resin (Sigma-Aldrich; components A and B, 33.3 g; components D and E, 1 g). Sections were dehydrated in aqueous solutions containing increasing concentration of ethanol (50%, 70%, 96%, 100%), prior to placing tissue into a 50% durcupan - ethanol mix. The mix is then replaced gently with increasing concentration of durcupan, until reaching pure resin. Sections were left so overnight, then embedded in a thin layer of fresh resin in an aluminum weigh boat and place in a 60° oven for about 24 h.

2.2. 3View imaging

The following procedure is used to mount specimens to minimize specimen charging. Region of interests corresponding to somatosensory cortex were dissected under a stereoscopic microscope using a razor blade, then mounted on aluminum specimen pins (Gatan, Pleasanton, CA) using cyanoacrylate glue. The blocks are faced and precision trimmed with a glass knife to a square of approximately 0.5–1.0 mm side length, so that tissue is exposed on all four sides. Silver paint (Ted Pella) is used to electrically ground the exposed edges of the tissue block to the aluminum pin taking care not to get the paint on the block face or edges of embedded tissue that will ultimately be sectioned. The entire surface of the specimen is then sputter coated with a thin layer of gold/palladium (25 mA, 3 min). After the block is surfaced with the 3View ultramicrotome (Gatan, Pleasanton, CA) to remove the top layer of gold/palladium, the tissue can be imaged using BSE mode. The stack used for reconstruction resulted 1513 images, sections having been cut at 50 nm thickness, and side length is 101 μm . Micrographs were acquired using a FEI Quanta 200 SEM. Each image has 4096×4096 pixels, with a pixel size of 20 nm. The acquisition parameters of the microscope have been adjusted as the best tradeoff between quality of imaging and ultramicrotomy: high-vacuum mode, voltage 3 kV, current 75 pA, pixel time 7.5 ps, spot size 3, magnification 1500.

2.3. 3D reconstruction, proofreading and rendering

Serial micrographs were first registered using Multistackreg plugin, freely available on Fiji (Thevenaz et al., 1998). Neurons and glial cells

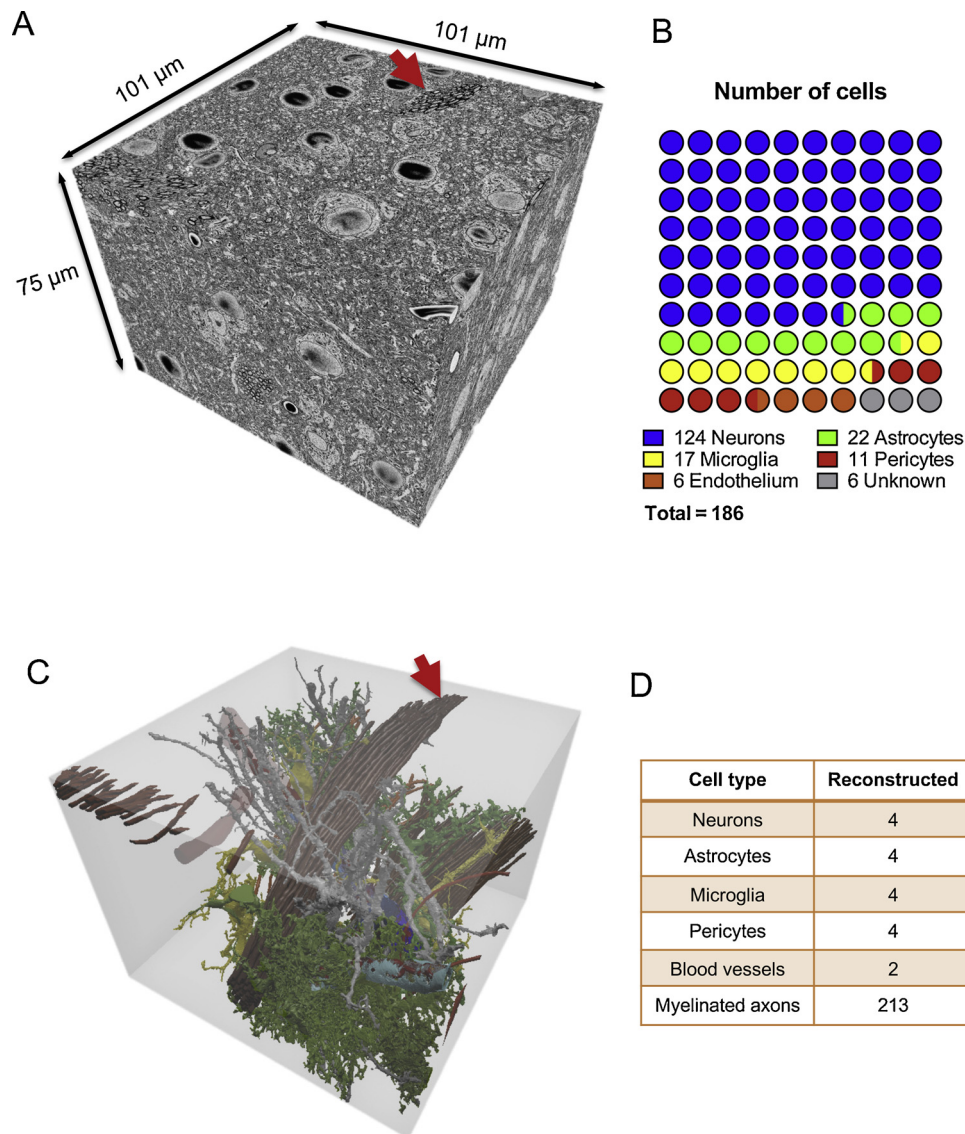


Fig. 1. Volume imaging and cell counts from Layer VI Somatosensory cortex. (A) Serial-Block Face volume rendering. Red arrow points to one group of myelinated axons used as a reference for the orientation of the 3D reconstruction in (C). (B) Visual representation of the counts of nuclei, per type, present in the imaged volume. (C) Sparse 3D reconstruction of the structures, indicated in (D). Grey, neurons; green, astrocytes; yellow, microglia; blue, pericytes; red, blood vessel; brown, myelinated axons.

were then segmented using a hybrid pipeline involving TrakEM2 for manual segmentation, as well as proofreading, and a version of iLastik that use TrakEM2 masks as seeds for semi-automated segmentation (Holst et al., 2016). Mitochondria, blood vessels and cells nuclei were automatically segmented. For blood vessels and nuclei, we used iLastik on a downsampled version of the stack. The models extracted from these two software were then imported and rendered using Blender. Images were processed using Adobe Photoshop to adjust brightness, contrast, and add pseudo colors to highlight structures of interests.

2.4. Analysis

All analyses were performed using Graphpad Prism 6. All data are expressed as mean \pm SE of the mean, and error bars represent SE. Quantifications on volume data (volume measurements, skeletons) or surface meshes (surface area and length measurements) were performed using Avizo, or custom tools python-coded for Blender based on Neuromorph (Jorstad et al., 2015), respectively. Sphericity of the nuclei was calculated using the following equation:

$$\Psi = \frac{\pi^{\frac{1}{3}} (6V_n)^{\frac{2}{3}}}{SA_n}$$

where V_n and SA_n are the volume and surface area of the nuclei, respectively. Maximum and minimum axis of the nuclei were obtained by fitting an oriented bounding box around each of the nuclei, using a custom script.

Quantifications on mitochondrial distribution, and qualitative visual assessments using Virtual Reality (VR) were based on the GLAM algorithm (Agus et al., 2018a; Cali et al., 2017). Specifically, we modelled mitochondria as emitting surfaces, and we evaluated energy absorption on the surrounding processes according to a vertex-based radiance transfer scheme. For each vertex x^p of the 3D surface reconstruction of the cellular process, the absorption value is computed by considering the KNN mitochondria vertices x_i^m according to the following equation

$$p(x^p) = \sum_{i \in \text{KNN}(x^p)} K_i e^{-|x^p - x_i^m|}$$

In this way, we were able to map the localization on the processes

according to the halo projected on the membrane in form of absorption map. We then evaluated the highest absorption peaks and we marked them as spheres with varying radii. To evaluate their length and radii, mitochondria were fed into an automated custom-made pipeline that skeletonized the morphologies from the meshes and calculated the length and radii of individual tubules.

2.5. Reagents

All chemicals used were from Sigma-Aldrich, unless otherwise specified.

2.6. Limitations

Electron microscopy is still the only method available to resolve details at nanometer resolution. It is therefore the technique of choice in neuroscience to study synapses and intracellular organelles (Knott and Genoud, 2013). Nevertheless, the treatments used to render a tissue sample suitable for EM imaging are known to create severe cellular and extracellular artifacts. Extracellular space which is estimated around 20% of the *in vivo* brain volume, drops to 1–2% when imaged under EM (Nicholson and Hrabětová, 2017) – most likely due to swelling of astrocytic processes during perfusion. It has been shown that the use of high-pressure freezing, a technique using vitrification of the water present in the sample to fix the tissue, followed by freeze-substitution protocol better preserves the extracellular space. Under these conditions astrocytic processes appear qualitatively different from the ones in chemically fixed samples (Korogod et al., 2015), suggesting that the latter preparation might not be suited for an in-depth analysis of the ultrastructure of these cells. While high-pressure freezing might seem ideal for ultrastructural studies, it cannot be used reliably to preserve large samples that are hundred microns thick, leaving no other choice to date but to use chemically fixed tissue. Moreover, since high-pressure freezing has not yet been applied systematically to various brain structures, it is not clear if the ground-truth representing the real cellular ultrastructure can be determined with this technique.

3. Results

From an imaged total volume of 750,000 cubic microns (Fig. 1A; $100 \times 100 \times 75 \mu\text{m}$), we segmented and reconstructed in 3D a total of 16 cells, including their cell bodies, out of 186 in total (Fig. 1B), two blood vessels and 213 myelinated axons (Fig. 1C and D; Supplementary Video 1).

3.1. Cell classification

The total number of cells present in the volume was calculated by reconstructing all the nuclei present in the stack. The total cell density was therefore evaluated as 220,000 cells per cubic millimeter. A total number of 186 cells were present in the cube. The type of cell was then classified by visual assessment by looking at specific morphological traits (Table 1; Fig. 2). We classified five major types of cells (Supplementary Table 1): 124 neurons, 22 astrocytes, 17 microglia, 11 pericytes, 6 endothelial cells, and 6 of an unidentified, unknown cell type, most likely oligodendrocytes, oligodendrocytes precursors (OPC), or NG2 cells (Butt et al., 2002; Chelini et al., 2018). Nuclei can be also automatically classified by approximating their shape with appropriate fitting functions, such as hyperquadrics or spherical harmonics, and by analyzing the parameters of these functions (Agus et al., 2018c, 2019b).

Neurons were identified by the presence of a dendritic arborization developing from the soma (the proximal dendrites), and most importantly by the presence of spines and synaptic contacts (Fig. 2A). Their nuclei are almost spherical, and on average largest among the studied cell types (Fig. 3C, D). Interestingly, all neuronal nuclei in this sample show a dark artefact typical of electron accumulation in

Table 1
Qualitative features for visual assessment of brain cell types.

Cell type	Nucleus	Soma	Processes	Other Distinctive Traits	Cytosol
Neuron	Round	Regular, rather round, depending on neuronal type (e.g. pyramidal neurons have a triangular cross-section next to the proximal dendrite)	Axons and dendrites; regular round cross-section	Synapses	Clear
Astrocyte	Round or irregular	Very little cytosol around the nucleus; perisomatic process rich in organelles, especially mitochondria.	Variable cross-section, undefined shape high tortuosity, mitochondria in larger processes (above 200 nm)	Perivascular processes	Clear
Microglia	Flattened	Irregular shape, flattened, with concavities and convexities.	Regular, round cross-section, average tortuosity	/	Clear or darkened
Unknown (OPC or Oligodendrocytes)	Round, regular	Rich in ER	Round regular cross-section, similar to microglia	/	Dark
Pericyte	Flattened, thin, convex toward the vasculature	Flattened, convex, very little cytosol around the nucleus	Flattened, thin, rich in mitochondria	Convexity towards astrocytic perivascular processes, concavity towards endothelium	Dark
Vascular Endothelia	Flattened, thin, convex toward the vasculature	Flattened, convex, very little cytosol around the nucleus	Flattened, thin, rich in mitochondria, directly facing the lumen of the vasculature	Convexity towards pericyte, concavity towards vasculature	Dark

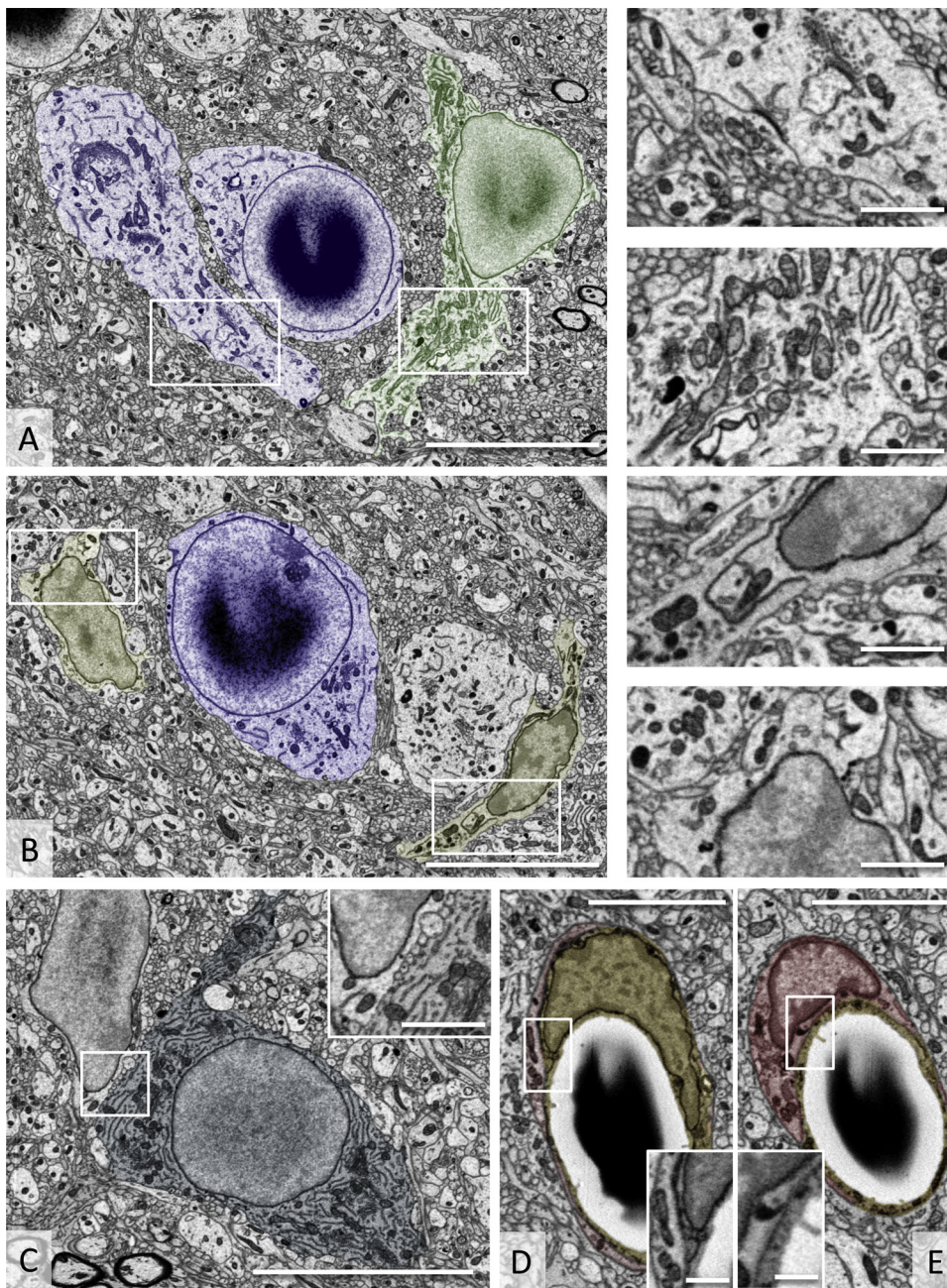


Fig. 2. Cell type recognition from single micrographs. (A) Micrograph showing one neuron (blue) and one astrocyte (green). Neurons can be recognized by presence of synapses (right, top panel), astrocytes by a massive concentration of mitochondria and ER in proximity of the soma of the cell (right, bottom panel). (B) Micrograph showing one neuron (blue) and two microglial cells (yellow). Microglia (right panels) can be recognized by a slightly darker cytosol, and presence of thin straight processes with a fairly regular diameter. (C) Oligodendrocytes or OPC (dark green) have a darker cytosol, but are considerably bigger compared to microglia, and their soma is very rich in ER. (D), (E) Pericytes (red) are facing the brain parenchyma from their convex side, and the vasculature endothelium (yellow) from their concave side. Scalebars: A,B,C, main panels, 10 μm ; insets, 2 μm ; D,E, main panels, 5 μm ; insets, 1 μm .

portions of the sample where there is low density of material, and therefore are poorly conductive, similar to the lumen of the blood vessel (Supplementary Fig. 1).

Astrocytes, unlike neurons, do not show specialized domains along their processes, to allow recognizing them readily. Their cytosol is generally clearer than that of neurons or other types of glia (microglia), but the largest processes rising directly from soma are typically packed with intracellular organelles such as ER and mitochondria. The absence of synaptic contacts, the high branching order resulting from many small processes intermingled within the neuropil, and the presence of at least one perivascular endfoot, are some distinctive traits of astroglial cells. Their nuclei have an irregular shape and they are smaller than in neurons (Fig. 3C, D; Supplementary Table 2).

Microglial cells were identified by the presence of branches that appeared regular in size and direction, without the extensive branching seen in astrocytes along their path. Also, 35% of the total microglial cells in the imaged volume has a cytosol darker than in neurons and

astrocytes, a condition seen before (Bisht et al., 2016). The size of their nuclei is smaller than neurons and astrocytes and their shape is irregular and highly diverse among individual microglial cells, depending on the shape of their soma which might need to flatten in order to move within the neuropil.

Vasculature was easy to identify as a hollow round pipe crossing the image stack. There are two cell types wrapped tightly around the vessel: the endothelial cells and the pericytes.

Endothelial cells are very easy to identify, as they are directly facing the lumen of the blood vessel and are therefore in direct contact with the blood flow. Their nuclei are also flattened, but have a regular, round shape if looked from the x-axis, giving them the appearance of a "potato chip" in 3D, confirmed by a small sphericity index (0.67; Fig. 3C). Endothelial cells have a dark cytosol, and their cross-section is flat and thin, roughly ranging from 300 nm (in portions without organelles) up to 4 μm (in correspondence of the thicker portion of the nucleus). The average size of the nuclei was the smallest among all those analyzed,

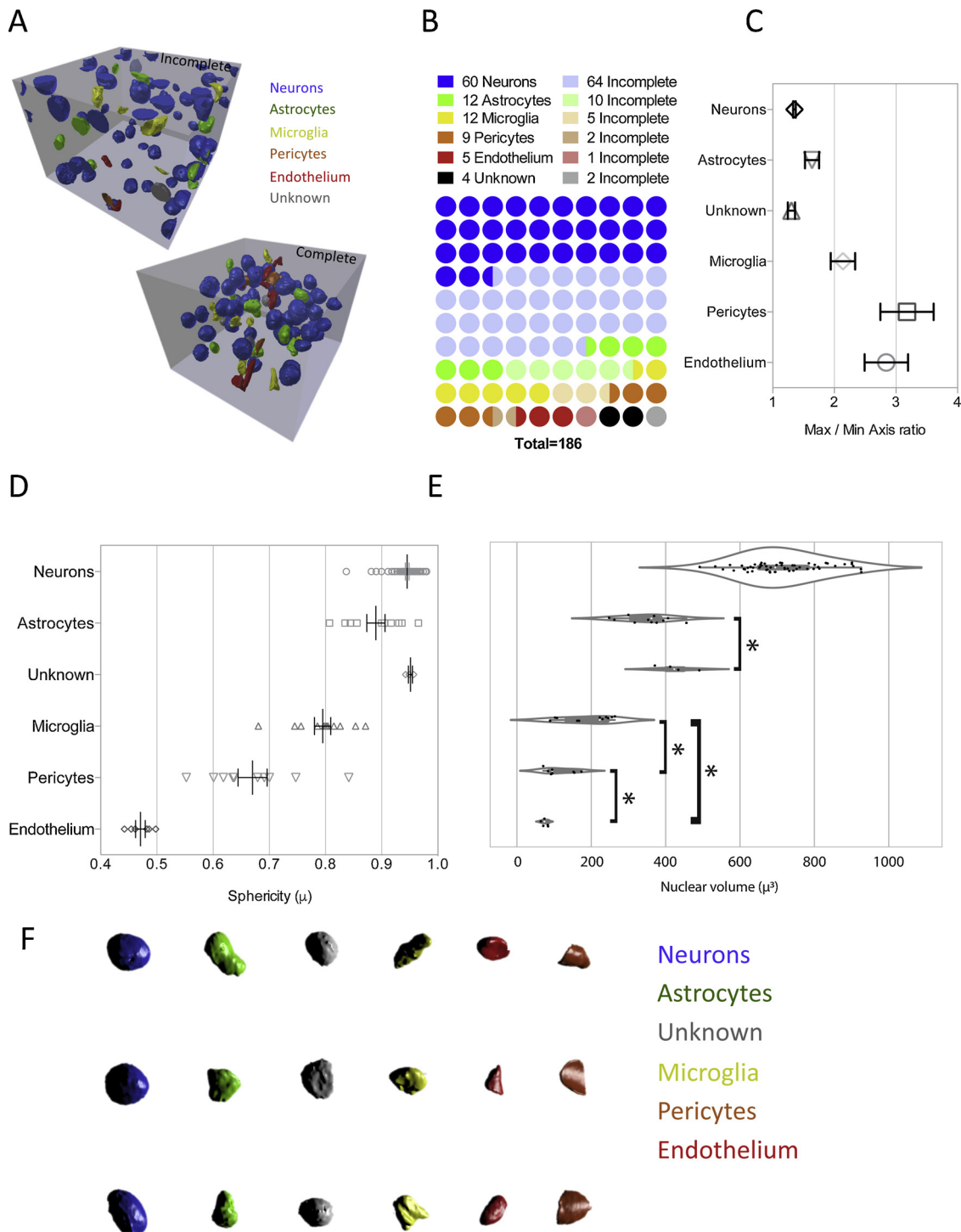


Fig. 3. Characterization of nuclei per each cell type. (A) 3D reconstruction of all the nuclei present in the imaged volume, color-coded per cell type. Only the complete ones (bottom) have been used for volume measurements. (B) Quantification and graphical representation of number of nuclei in (A), clustered per cell type. (C) Average Max / Min axis ratio per each type of nuclei. (D) Sphericity of the nuclei, grouped per each cell type. (E) Quantification of the volume of reconstructed nuclei, grouped by statistical similarity. *One-way ANOVA, Holm-Sidak multiple comparison test, $P > 0.05$. (F) A selection of reconstructed nuclei highlights their morphological diversity.

together with the smallest sphericity index (0.47; Fig. 3C). Pericytes sit on top of endothelial cells from one side, and interface with the astrocytic endfoot on the other side. They have a very tight, dark, electron-dense membrane interfacing with the endothelium, and have as well a very dark cytosol similar to endothelial cells.

Lastly, so called "unknown cells" (4 in total) have a dark cytosol and their soma is filled with smooth ER. Their morphology is reminiscent of

oligodendrocytes or their precursors (OPC) which, given the development stage of the brain sample (P14), are more likely.

3.2. Nuclei

Out of 186 nuclei, 102 were entirely within the volume (Fig. 3), therefore we measured the volume and sphericity of each nucleus and

compared them, grouping by cell type (Supplementary Table 2). Neurons had the largest nuclei ($715.7 \pm 13.01 \mu\text{m}^3$, $N = 60$), followed by astrocytes ($349.3 \pm 18.88 \mu\text{m}^3$, $N = 12$) and unknown cells ($427 \pm 24.9 \mu\text{m}^3$, $N = 4$), last two being statistically similar (Holm-Sidak's multiple comparison test; $t = 1.54$). Those three cell types had also the highest sphericity, an index of how close is the shape of a particle to a sphere of a certain volume (neurons, $0.9455 \pm 0.003 \mu\text{m}$, $N = 60$; astrocytes, $0.8895 \pm 0.016 \mu\text{m}^3$, $N = 12$; unknown, $0.9512 \pm 0.003 \mu\text{m}$, $N = 4$). Nuclei of microglia ($185.5 \pm 18.7 \mu\text{m}^3$, $N = 12$), pericytes ($120.1 \pm 13.3 \mu\text{m}^3$, $N = 9$) and endothelial cells ($75.3 \pm 3.6 \mu\text{m}^3$, $N = 5$) were similar (Holm-Sidak's multiple comparison test; microglia vs pericytes, $t = 1.72$; microglia vs endothelial cells, $t = 2.402$; pericytes vs endothelial cells, $t = 0.9316$), with a sphericity further from 1 (*i.e.* perfect sphere), endothelial nuclei being the lowest (microglia, $0.7949 \pm 0.014 \mu\text{m}$, $N = 12$; pericyte, $0.6703 \pm 0.025 \mu\text{m}^3$, $N = 9$; endothelium, $0.4707 \pm 0.008 \mu\text{m}$, $N = 5$). These observations were confirmed by evaluating the maximum and minimum axis of the nuclei (Supplementary Table 3), with pericytes and endothelium showing a ratio (Fig. 3C) of 3 between the two (endothelium, 2.83 ± 0.35 ; pericytes, 3.18 ± 0.43). Microglia was somehow in between (2.14 ± 0.19), while neurons, astrocytes and unknown cells had a ratio closer to one (neurons, 1.34 ± 0.02 ; astrocytes, 1.63 ± 0.11 ; unknown, 1.3 ± 0.05).

3.3. Surface area to volume ratio

Both surface area, and volume of each reconstructed morphology (Fig. 4A), were calculated; nevertheless, because of the total volume sampled was not sufficient to contain the complete structure of the identified neurons and astrocytes, comparing absolute numbers was not feasible. We therefore decided to evaluate surface area-to volume ratios, which can be considered as a measure of how much the morphology of a cell is adapted to interact with its environment (Supplementary Table 4). Neurons and microglia have little statistical difference (neurons, 1.63 ± 0.05 ; and microglia, 2.8 ± 0.3 , $N = 4$, $p < 0.05$), whereas astrocytes and pericytes have higher ratios, and are not significantly different (astrocytes, 4.39 ± 0.3 ; and pericytes, 4.26 ± 0.09 , $N = 4$) (Fig. 4B). Interestingly, linear regressions of surface areas versus volume graphs (Fig. 4C) show that in this respect astrocytes and pericytes are very similar to each other (they fit on the same slope, $R^2 = 0.97$), and neurons and microglia match each other ($R^2 = 0.94$).

3.4. Astrocytes

Astrocyte data was subjected to a number of qualitative assessments, and their features of interest were quantified. First, by applying the same thinning algorithm to the 3D volume data of the segmented astrocytes we could extract a GFAP-like morphology that allowed visual identification of their soma and main processes (Fig. 5B). Each of the four astrocytes have 4 primary processes branching out from the soma. By analyzing the skeletons, we found that these astrocytes have 1853, 6001, 6240 and 1853 branches, respectively (Fig. 5C). The number of branches correlates with the size of the cell (See Fig. 4C).

For each astrocyte, we have calculated a maximum and minimum radius by fitting an ellipsoid to encompass the outer surface of the cell and centered in the nucleus of each astrocyte. In order to make a rough estimate of the percentage of cell reconstructed, as all astrocytes have processes cut at the boundary of the image stack, we have assumed that the cells are roughly symmetrical, and have calculated the percentage of the volume of the fitting ellipsoid lying within the bounding box. We found that astrocytes 1 and 2 are the least complete ones (52% and 66% complete, respectively), followed by astrocytes 3 and 4, both complete at 78%.

Of the four reconstructed astrocytes, three of them (1, 3 and 4) have two perivascular processes (example from astrocyte 1 in Fig. 6A); the

remaining cell (number 2) is lying on a bifurcation, hence its one perivascular process has larger surface area than in the other three astrocytes (Fig. 6B, empty square). The surface area of the process facing the lumen of the blood vessel was quantified using the blender addons family Neuromorph, and the ratio with the volumes of the processes (Fig. 6C; Supplementary Table 5), which in all seven cases appeared as a thin, flat, curved surface, was between 1 and 2.5. Indeed, linear regression from the volume-surface area representation of the data (Fig. 6B, red dotted line) had a coefficient close to 1 (0.97).

3.5. Neurons

Four neurons were randomly selected out of the 124 present in the stack whose nucleus was complete, segmented and their morphology reconstructed in 3D (Fig. 7A). They had between 4 and 7 proximal dendrites, with neuron number 2 not showing any axon, possibly because the process is cut at the proximal portion of the neuron. Although neuron number 1 had the smallest number of spines within the imaged volume (262), it had the highest total dendritic length (816.1 μm), and the longest dendrite (106.7 μm) compared to the other neurons. Consequently, its spine linear density (Fig. 7B) was significantly different compared to the other 3 neurons (#1, 0.35 ± 0.033 spines/ μm ; #2, 0.71 ± 0.06 spines/ μm , $p < 0.001$; #3, 0.62 ± 0.06 spines/ μm , $p < 0.01$; #4, 0.54 ± 0.05 spines/ μm , $p < 0.05$). A similar analysis was performed on the surface density of spines, by calculating the volume of individual dendrites, and the results revealed the same trend (Supplementary Table 6). Linear regression of the dendritic volumes versus number of spines indeed confirm that neuron 1 differs from the other ones. We evaluated the minimum and maximum radius, by placing a sphere in the soma of each neuron until it reached the shortest and longest process of each cell, respectively. In all cases, the maximum radius was close to the longest dendrite of each neuron.

3.6. Pericytes and vasculature

Four pericytes out of 11 were reconstructed in 3D (Fig. 8). The reconstructed ones (Fig. 8B) have a thin cytosol, and most of their surface is either facing the endothelium surrounding the lumen of the blood vessel, or the neuropil on the opposite side. Since pericytes do not have a clear symmetry around their nuclei, we have calculated their maximum and minimum axis from their bounding box. Pericyte 2 and 3 are both lying on a bifurcation, and are also the ones with the highest occupancy, with a maximum axis of 42.1 and 45.7 μm , respectively.

Two vasculature segments were found in the sample, showing a black artefact in the middle of their lumen due to the imaging technique that is inducing electron accumulation within empty resin. The largest segment is 103 μm long (segment 1), and cross the entire image stack on the z-axis. Another segment (number 2) is 49.45 μm long, from which another bifurcation departs (segment 3), at the top of which astrocyte 2 is lying (Fig. 5A).

By observing the location of nuclei, it was possible to estimate the density of pericytes along the length of the blood vessel (Fig. 8C). We found a positive correlation with the density and the diameter of the vessel.

3.7. Microglia

Four microglial cells out of 17 were reconstructed in 3D (Fig. 9). The morphology of the four cells varies strongly, although number 2 and 3 have close number of total branches (54 and 49, respectively) and their total volume is quite similar ($545 \mu\text{m}^3$ and $550 \mu\text{m}^3$, respectively). The number of branches has a non-linear correlation with the volume of the cells (Fig. 9B), but does not appear to be correlated with their surface area (Fig. 9C; Supplementary Table 7). To evaluate the occupancy of each cell, we evaluated the minimum and maximum radius, by placing a sphere in their soma until it reached their shortest and longest

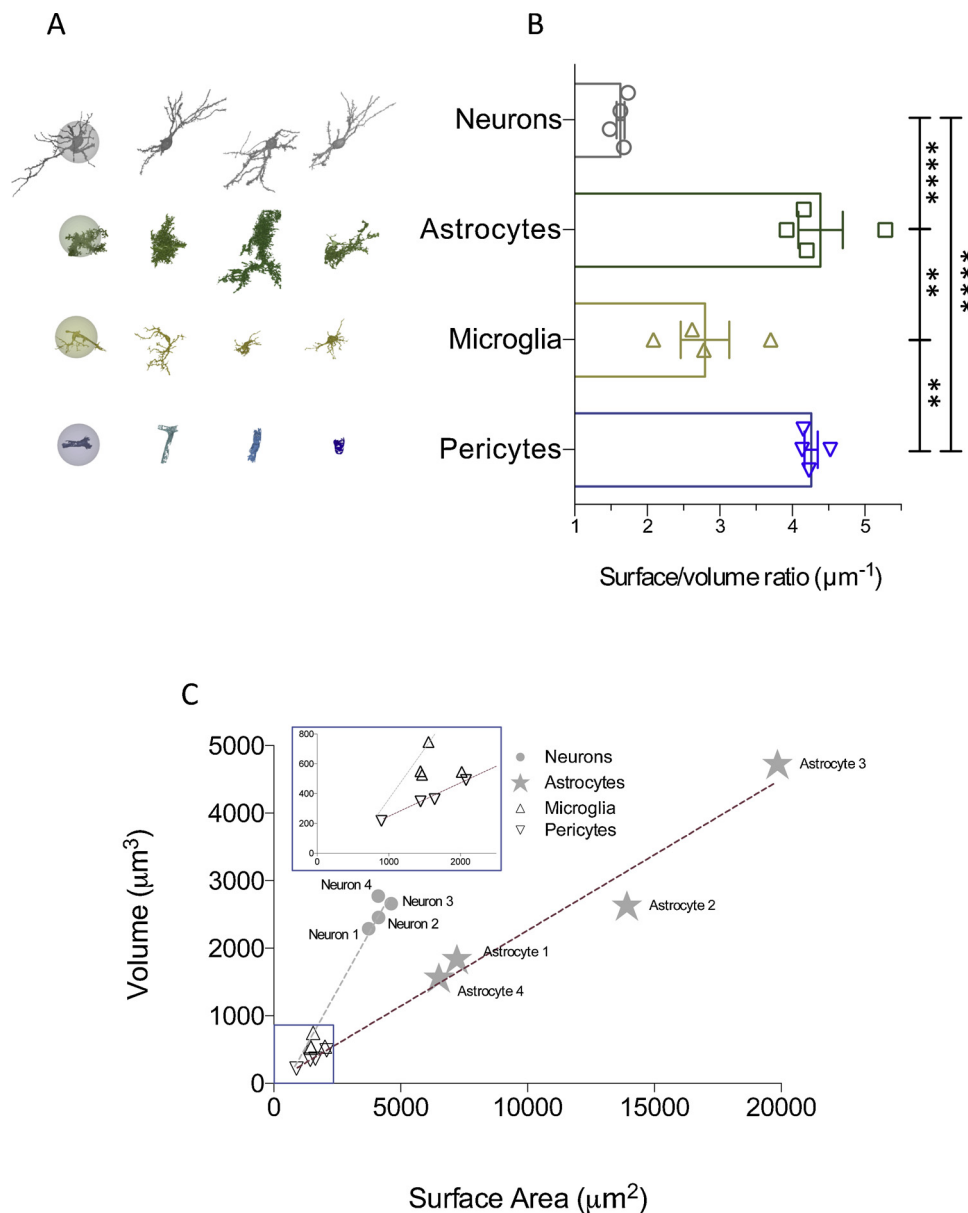


Fig. 4. Surface area to volume ratio in reconstructed cells. (A) Rendering of all the reconstructed morphologies for subsequent quantification. Spheres centered around the somas on the first column have a diameter of 50 μm . (B) Quantification of SVR per each cell type. One-way ANOVA, Holm-Sidak multiple comparison test; ** $P < 0.01$; **** $P < 0.0001$. (C) Linear regression of Surface Area v Volume per each cell.

process. We found that microglia 3 and 4 have the shortest minimum (7.7 μm and 7.8 μm respectively) and maximum (29.7 μm and 35.4 μm respectively) radii.

3.8. Mitochondria

All the mitochondria from the sample were segmented together, using an automated classifier that was trained on a manually segmented portion of the stack, and then various qualitative and quantitative analyses were performed based on cell and cell type distribution (Fig. 10; Supplementary Tables 8–10). The percentage of mitochondria per each type of cell calculated as a ratio between the volume of mitochondria and the volume of each cell (Fig. 10E) was not significantly different among the cell types, although quantification revealed a similar trend between pericytes and astrocytes, and neurons with microglia (pericytes, $9.6 \pm 1.57\%$; astrocytes, $8 \pm 1.1\%$; neurons, $7.3 \pm 0.4\%$; microglia, $6.4 \pm 0.4\%$; $N = 4$ per each cell group). From a qualitative point of view, the spatial distribution of mitochondria in

neurons and microglia (Fig. 10B and D, respectively) was similar, as it follows the skeleton of the cells from the nucleus to their distal processes. Within pericytes, mitochondria were evenly distributed within the cytosol (Fig. 10B), whereas in astrocytes (Fig. 10A) they followed the lines drawn by the major processes, and were particularly dense in the proximity of the soma and in the perivascular endfoot.

By using an automated skeletonizer, we have extracted quantitative information about the length and radius of mitochondria per cell type (Supplementary Tables 9 and 10), within their soma and their processes (Fig. 10F and G, respectively). In the soma, astrocytes had the longest average mitochondrial length ($2.23 \pm 0.11 \mu\text{m}$, $N = 203$), followed by pericytes ($2.13 \pm 0.15 \mu\text{m}$, $N = 125$) and neurons ($1.95 \pm 0.03 \mu\text{m}$, $N = 1036$), while microglia had the shortest mitochondrial average ($1.71 \pm 0.11 \mu\text{m}$, $N = 93$). In the processes, neurons had the longest mitochondrial average length ($2.86 \pm 0.08 \mu\text{m}$, $N = 1014$), followed by astrocytes ($2.61 \pm 0.05 \mu\text{m}$, $N = 1209$) and microglia ($2.23 \pm 0.10 \mu\text{m}$, $N = 258$), while pericytes had the shortest mitochondria ($1.9 \pm 0.06 \mu\text{m}$, $N = 317$).

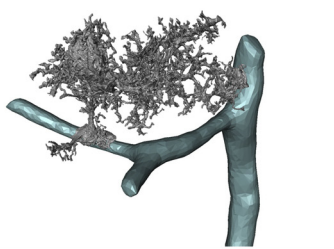
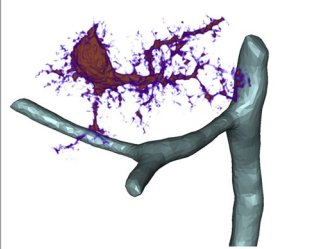
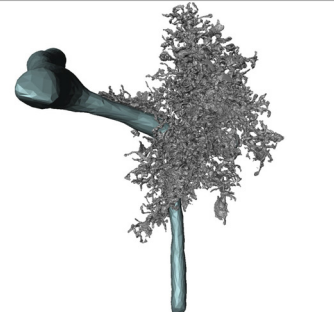

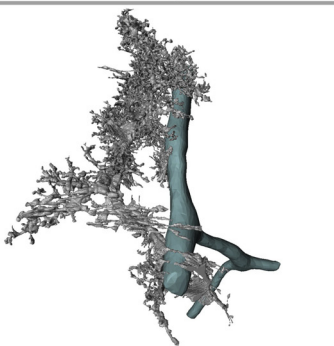
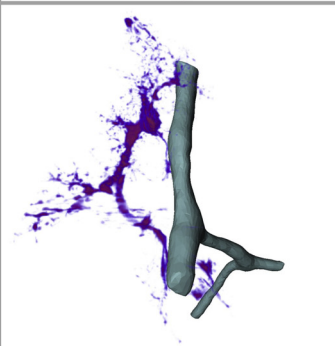
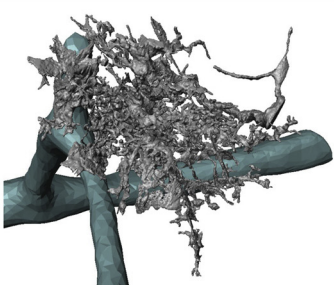
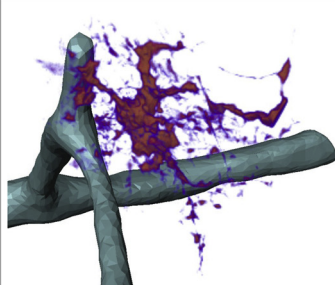
A	B	C
Full mesh	Thinned volume rendering	Qualitative Assessment
		Astrocyte 1 Primary processes: 4 Total Branches: 1853 Perivascular processes: 2 Max radius: 27 μm Min radius: 9 μm % Complete: 52
		Astrocyte 2 Primary processes: 4 Total Branches: 6001 Perivascular processes: 1 Max radius: 17 μm Min radius: 14 μm % Complete: 66
		Astrocyte 3 Primary processes: 4 Total Branches: 6240 Perivascular processes: 2 Max radius: 67 μm Min radius: 31 μm % Complete: 78
		Astrocyte 4 Primary processes: 4 Total Branches: 1853 Perivascular processes: 2 Max radius: 45 μm Min radius: 23 μm % Complete: 78

Fig. 5. Assessment of astrocytes morphology from their 3D reconstruction. (A) Full mesh rendering extracted from volume segmentation. (B) Volume rendering from thinning procedure to highlight primary processes. (C) Quantification of morphological parameters.

Finally, in order to easily infer the intracellular distribution of the mitochondria, and overcome the visual occlusion caused by the cellular complexity, we adopted a strategy similar to GLAM glycogen mapping (Agus et al., 2018b; Cali et al., 2017). We considered mitochondria as light sources, mapped their localization on the processes based on the halo projected on the membrane, and reported the highest absorption peaks as spheres (Fig. 11 A and B). We then proceeded to count the number of peaks (Fig. 11B) in different cell compartments, per each cell type (Fig. 11C). Virtual Reality (VR) was used to better understand the data (Supplementary Video 3). We found that in the vast majority of the cases high-density peaks were found along cellular processes rather than in the somatic part of the cell. As pericyte morphology is best described in relation with the lumen of the blood vessel (inside), or the parenchyma (outside), these terms were used in describing the location of the peaks.

3.9. Myelinated axons

Axons in EM micrographs have a well-known morphology. They show a relatively straight, tubular structure (Shepherd and Harris, 1998), with a tortuosity depending on the axonal type and swelling at sites, called boutons, where spheroidal vesicles accumulate. Myelinated axons have a much less convoluted path, a more regular and larger diameter compared to non-myelinated axons. Myelinated processes are large and smooth, and present a thick, dark electron-dense sheet around their circumference (Kreshuk et al., 2015).

We reconstructed a total of 240 myelinated axons, organized in four major bundles of 42, 30, 18 and 120 axons, as well as 3 fibers that were isolated and appeared clustered. The total length of the reconstructed fibers was 11,295 μm , with an average length per bundle of 97.63, 10.47, 75.51 and 44.89, respectively, all with a standard error between

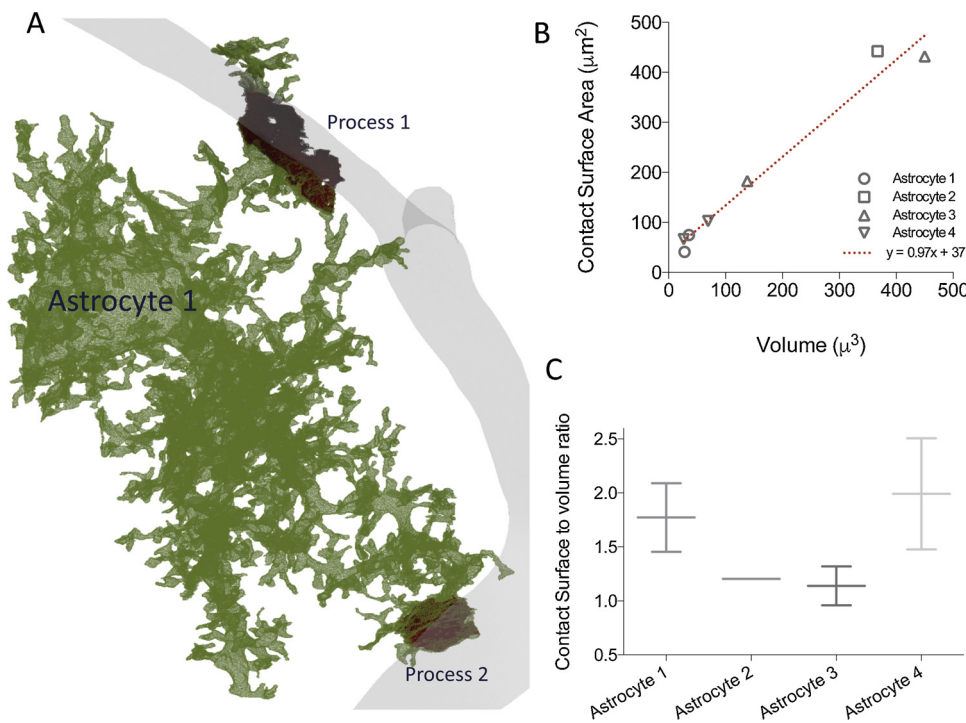


Fig. 6. Analysis of astrocytic perivascular arrangement. (A) Rendering of one of the reconstructed astrocytes with a detail from its two perivascular processes (red). (B) Quantification of the perivascular surface area (shown in A in red as an example). (C) Ratio between surface area of the contact and the volume of the perivascular process.

1 and 3% (Supplementary Fig. 2). All the fibers were crossing the stack at approximately 45° , considering the z direction to the proximal dendrite of neuron 1. Location and orientation of the sample together with the number of axons prompt us to assume that they originate from corpus callosum (Supplementary Video 2).

4. Discussion

The aim of this work was to provide for the first time a detailed description of the three-dimensional morphology of glial cells, with a particular emphasis on astrocytes, a dataset that is still largely lacking in literature with a few exceptions (Cali, 2017) and to adapt the tools originally developed for neuronal image segmentation, reconstruction and analysis to glial cells.

4.1. Cell recognition

The first challenge was to recognize the different categories of cells using EM. Ultrastructural analyses at the EM level are usually carried on in brain neuropil, and analyses on larger fields of view are limited to neurons. Although there is a general consensus regarding recognition of neurites and postsynaptic densities (PSDs), as well as their type (Shepherd and Harris, 1998; Stuart et al., 2016), it is rare to find similar definitions for other brain cell types, such as glial cells and the endothelium of the blood vessel (Table 1). This is despite the fact that endothelial structures are very simple to identify, as they are facing the blood vessel lumen (Fig. 2D,E). For glial cells, there is much less consensus, probably due to limited literature.

Comments on astrocyte structure in EM tend to be general and often misleading. Commonly, they are referred as empty structures with a relatively clear cytosol (Witcher et al., 2010, 2007); this misconception is probably due to the fact that investigations on astrocytic ultrastructure in the last twenty years have been mostly focused on gliotransmission, meaning on the ultrastructural features in astrocytes that could subserve the release of signaling molecules (Cali, 2017). These studies have looked at perivascular, lamelliform processes on separate 2D images, which might appear clear and empty, depending on the section shown. In reality, larger processes are full of organelles, such as

ER and mitochondria, that we observed in close proximity of the soma (Fig. 2A). Furthermore, perivascular processes (Mathiisen et al., 2010; Fig. 6) appear more complex than expected, showing local synthesis machinery such as the Golgi apparatus (Boulay et al., 2017), as well as glycogen granules (Agus et al., 2019a; Cali et al., 2016).

Microglia are very mobile cells that patrol their neighborhood in search of inflammations (Nimmerjahn et al., 2005), and have recently been shown to be responsible for synapse pruning (Thion and Garel, 2018). Microglia squeeze through other cells in brain parenchyma. Their morphology is adapted to that and these cells are easy to identify by the small size of their soma (Fig. 2B) and the convoluted shape of their nucleus (Savage et al., 2018). Interestingly, 6, out of the 17 microglia identified in the stack had a darker cytosol than other cell types. This phenotype has been reported previously (Bisht et al., 2016; Savage et al., 2018) and associated to a possible activated state of the cell. First reports about dark cells date back to Peters (Murakami et al., 1997); this observed phenotype was not limited to microglia, but also to so called “dark neurons”, as well as other cell types, similar to another category of cells that we found and referred to as “unknown”. Compared to the dark microglia observed, these cells have an even darker cytosol, and are probably oligodendrocytes or OPC (oligodendrocytes precursors).

Comparison of cell numbers between glial cells (astrocytes, microglia, pericytes and unknown, together) and neurons is of interest (Supplementary Table 1). Although it was not our aim to make a stereological count, as the volume is probably too limited, the estimation based on the nuclei present in the sample results in 30% glia, the remaining 70% being neurons. Contrary to a popular misconception that astrocytes are the most abundant cell type in the CNS, the total number of glia does not surpass the number of neuronal cells. Estimations using isotropic fractionator, a technique evaluating cell numbers based on nuclear staining, show that the number of neurons is higher than that of glial cells in rodents and primates, and is the same in humans (Herculano-Houzel, 2014; von Bartheld et al., 2016). Interestingly, this ratio depends on the brain region: for instance, in the cortex, the glia to neurons ratio shows that there is more glia than neurons, which is the opposite than what we found. Two possible explanations have been presented: First, the density of neurons is heterogeneous across cortical

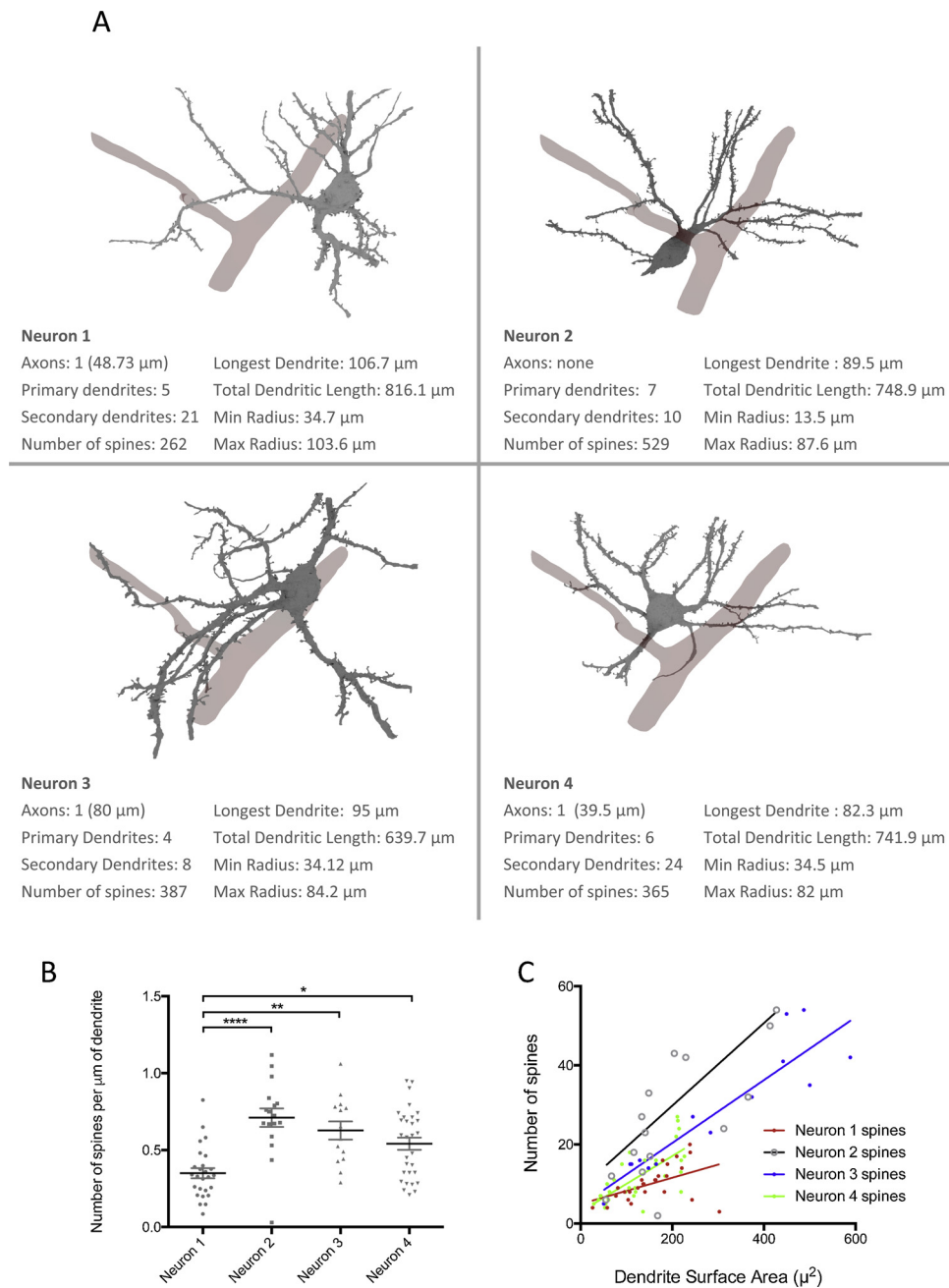


Fig. 7. Assessment of neuron morphology from their 3D reconstruction. (A) Renderings from the 4 reconstructed neurons, including parameters of interest. (B) Linear density of spines per each neuron. (C) Surface density of spines per each neuron, including linear regression.

layers. This is supported by data from layer I that has no (or very little) neurons, which means that by averaging numbers over entire cerebral cortex, the ratio could be unbalanced by the more glia in upper layers. Layers V and VI are known to have higher neuronal density (Santuy et al., 2018). Second, cellular densities of cells must change across developmental stages and the present data set is from a rapidly changing P14 brain.

4.2. Size of nuclei

All mammalian cells of one individual store the same genetic material in their nuclei. For rats, the Rat Genome Sequencing Project Consortium estimated the size of the rat genome to be 2.75 Gb, between human (2.9 Gb) and mice (2.6 Gb) (Rat Genome Sequencing Project Consortium, 2004), which, considering a weight of 660 g/mole-bp,

corresponds roughly to 7 pg of nuclear DNA within each normal diploid cell, although a recent report shows that human cell types might go well beyond that expected value (Gillooly et al., 2015). From a morphological point of view, we noticed differences in the appearance, both in 2D and in 3D, that we quantified by calculating the sphericity, an index of how close the shape of a particle is to a sphere (Supplementary Table 2). Nuclei from neurons, astrocytes and unknown cells had sphericity index closer to 1 (Fig. 3D), while pericytes and endothelial cells nuclei had the lowest, confirming the visual qualitative visual assessment of their shape. This observation matched the ratio between the maximum and minimum axis, (Fig. 3C; Supplementary Table 3) which was closer to one for the former group, and around 3 for the latter. Microglial cells, which are highly mobile and need to adapt their shape in order to migrate from site to site of the brain parenchyma, were somehow in between these two groups, showing some variability.

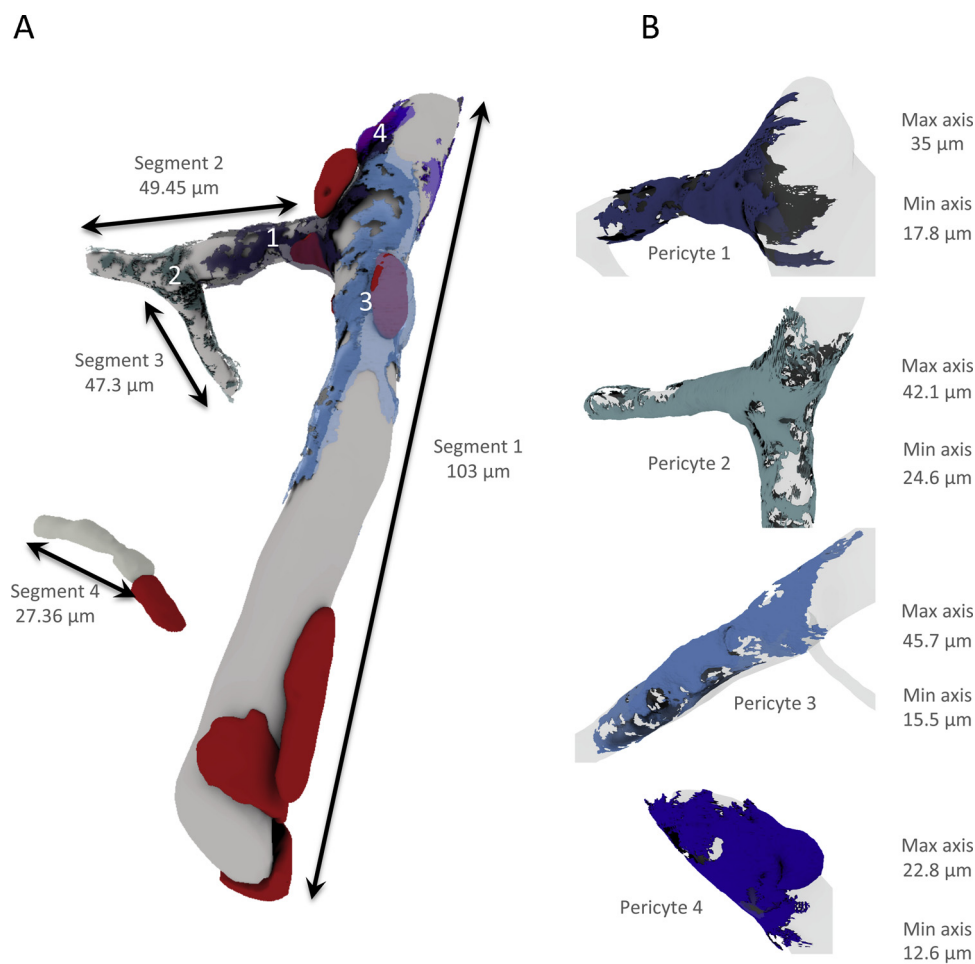


Fig. 8. Assessment of pericytes morphology from their 3D reconstruction. (A) Rendering of the reconstructed vasculature with the four reconstructed pericytes and the nuclei of all pericytes present in the volume (in red). (B) Rendering of individual reconstructed pericytes. (C) Quantitative relationship between pericytes and vasculature.

Interestingly, we found that by measuring the volume of nuclei of the different cell types (Supplementary Table 2), there was a substantial variability (Fig. 3E), with differences up to 10 fold, comparing the smallest nuclei (pericytes and endothelium, less than 100 cubic micrometers) with the larger ones (neurons, more than 900 cubic micrometers). If they all contain the same amount of genetic material, the difference must rely on the folding state of the cell, and possibly the expression of histone deacetylases and other epigenetic effectors, which are known to be affected during aging, and their impairment has been shown to favor phenomena like LTP, and improve long term memory and cognition (Cao et al., 2018; Maze et al., 2013; Penney and Tsai, 2014; Walsh et al., 2015; Shu et al., 2018) by having a more fluid

nucleus that facilitates the access of nuclear information to transcriptional factors, and therefore protein turnover (Maze et al., 2013). As a further proof of this point, an imaging artefact was useful to confirm that neuronal nucleus was less “dense”. As we imaged using back scattered electrons from the block surface of the tissue, in order to obtain images similar to the more familiar TEM ones, non-reflective, less conductive surfaces absorb electrons and therefore appear black. Notably, this occurs in the lumen of blood vessels, where there are no proteins, but where only resin is present, therefore no combination of osmium, lead and uranium can generate an image, because there is nothing to bind to. Interestingly, all the nuclei from neurons had at their core this black artefact (Supplementary Fig. 1), whereas none

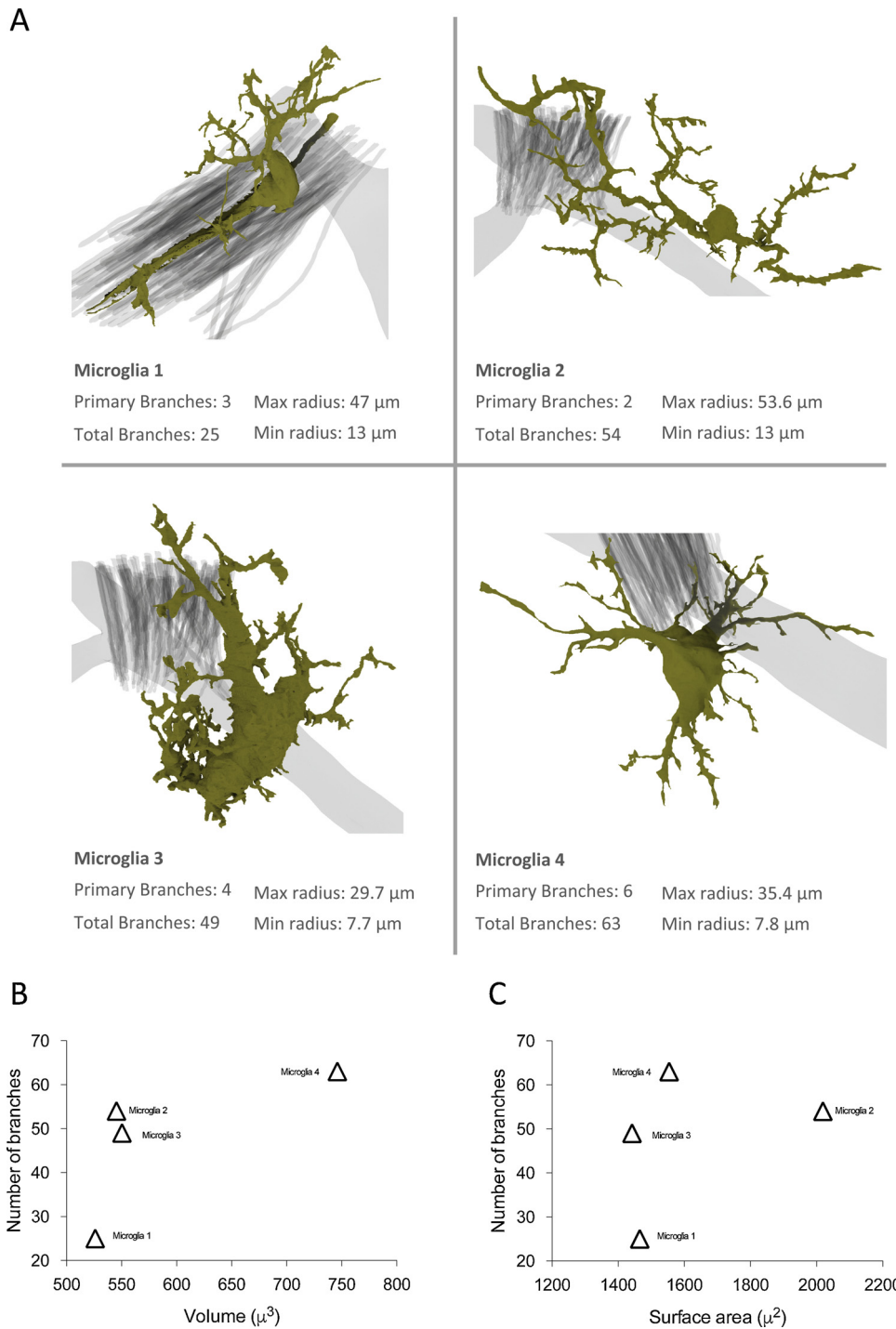


Fig. 9. Assessment of microglia morphology from their 3D reconstruction. (A) Rendering of the four reconstructed microglia, together with morphological parameters. (B) Number of processes plotted against the volume of each cell. (C) Number of processes plotted against the surface area of each cell.

from other cells, including the larger nuclei of astrocytes and microglia that matched in size the smallest nuclei of neurons, showed the same hallmark. This feature is peculiar for our sample preparation and our imaging conditions, and more recent SBEM setups have introduced systems to reduce substantially the charging using focal injection of nitrogen (Deerinck et al., 2018). We used this dataset to train shape analysis AI algorithms to infer cell type solely from the size and morphology of the nuclei (Agus et al., 2019b, 2018c). By comparing different methods of representation of the nuclei (hyperquadrics versus spherical harmonics), we could train a support vector machine classifier (SVMC) to distinguish between cell types, and found that neurons can

be distinguished with almost 100% accuracy, as different parameters clusters well together when plotted for dimension reduction, compared to other cell types (Agus et al., 2019b). SVMC can also classify astrocytes relatively well, although in some cases they can be mistaken for neurons; in contrast, other cell types have too high variability and automatic classifiers fails to distinguish them. By acquiring more dataset to enhance the accuracy of training, the SVMC might be a powerful tool to pre-assess the identity of a cell by its nucleus, which is easy to identify and segment.

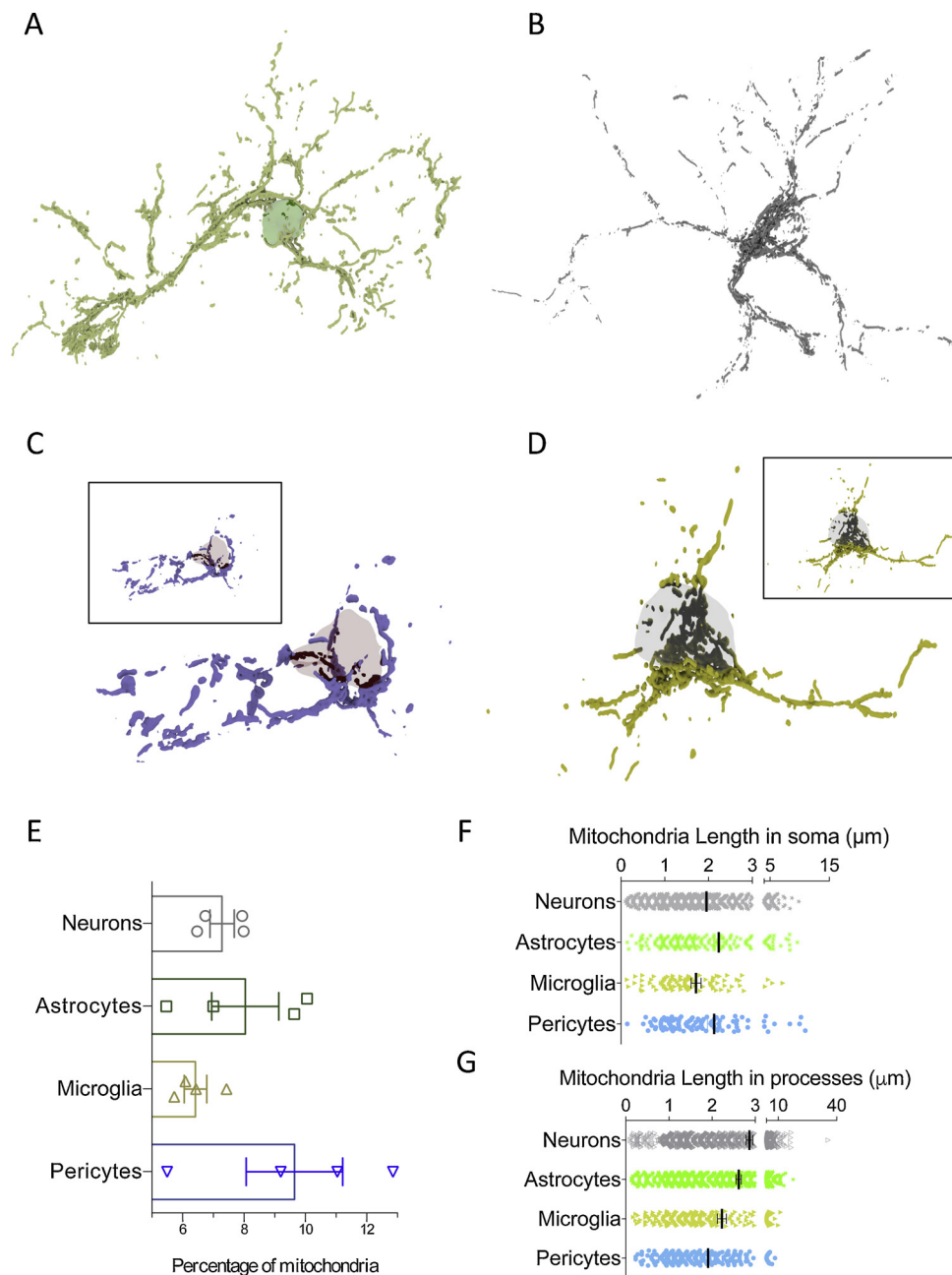


Fig. 10. Analysis on mitochondria distribution in different cell types. (A) Mitochondria in one astrocyte. (B) Mitochondria in one neuron. (C) Mitochondria in one pericyte. Box inset reveals the size of the cell compared to A and B. (D) Mitochondria in one microglia. Box inset shows the size of the cell compared to A and B. (E) Average volume occupancy of mitochondria per cell type. (F) Length of mitochondria in the soma of the reconstructed cells. (G) Length of mitochondria in the processes of the reconstructed cells. Bars indicate average \pm SE.

4.3. Individual morphologies

3D models of neurons are increasingly common but very little effort has been done to segment morphologies of other brain cells from EM, although recently developed algorithms, such as flood filling networks (FFNs; Januszewski et al., 2018) are not specific for one cell type and are generally used for dense segmentation, suggesting that they could be applied to glial cells (Harris et al., 2015). One possible reason is that neurons have a clear morphological compartmentalization (axons, dendrites, spines, boutons, PSDs), and the changes in these compartments can be directly correlated to functional changes; for instance, dendritic spines can become smaller or bigger, newer ones can form based on synaptic inputs. Such compartmentalization is less known for glial cells. In the absence of morphologically identifiable functional

domains, the few reconstructions of glial morphology present in literature have been produced to elucidate processes of neuronal physiology, rather than for studying astrocyte function per se.

In this study, we aimed to reconstruct detailed individual morphologies of cells included in an imaged cortical volume. We first compared surface area to volume ratio (SVR) of different reconstructed cells (neurons, astrocytes, microglia and pericytes) as measured by their three-dimensional morphology (Fig. 4B). In contrast to absolute volume or surface area values that are not very informative (Fig. 4C), SVR is an indication of the fractality of the cell, and indicates how much a cell would sacrificing its intracellular volume to “dedicate” surface for interacting with its neighbors (Supplementary Table 4). It is not surprisingly then, that small pericytes have high SVR values (around 4), similar to astrocytes, while neurons and microglia (Fig. 4B) have lower

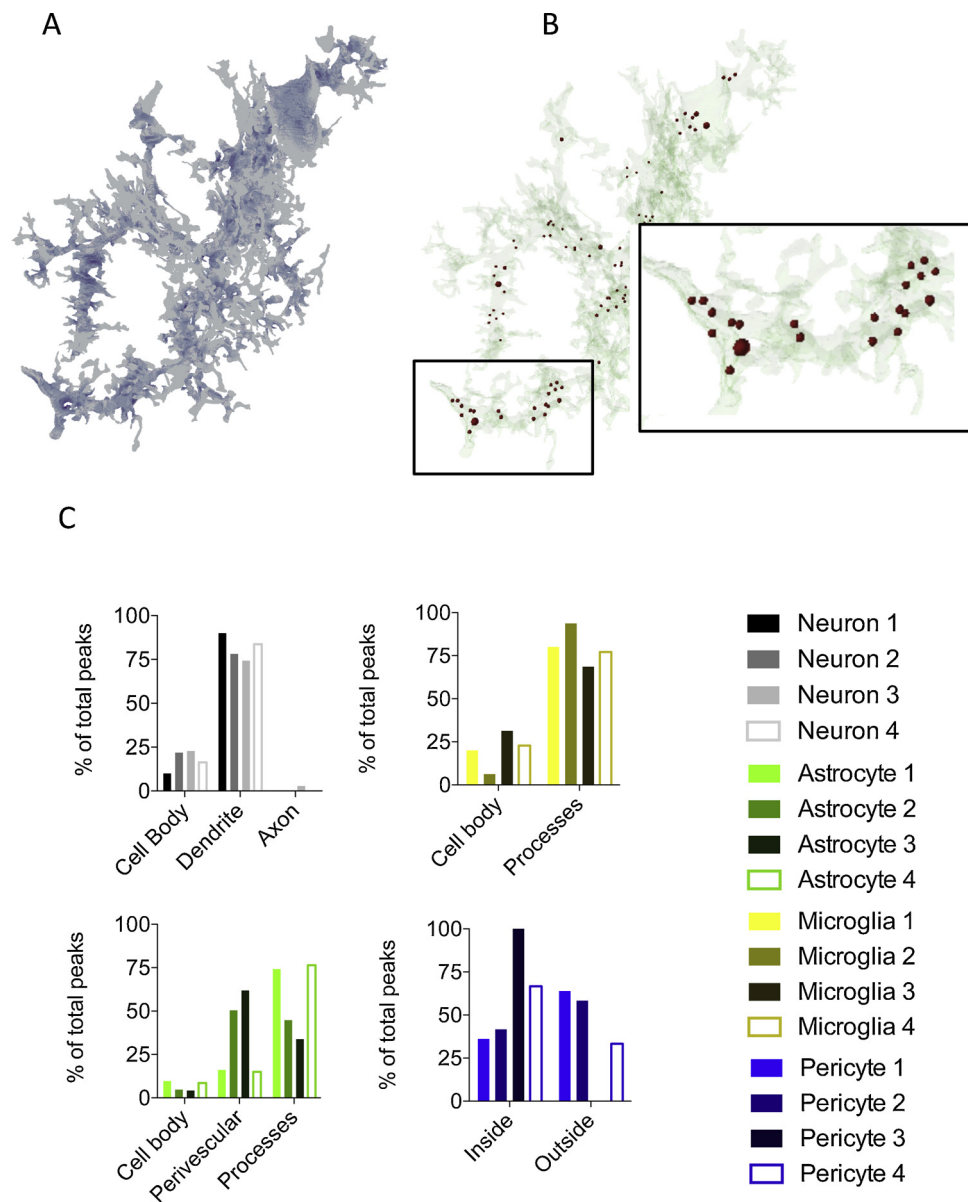


Fig. 11. Qualitative analysis of mitochondria distribution in different cell types using VR. (A) Example of an astrocyte where the surface has been mapped with color-coded peaks depending on energy-radiance paradigm based on the below mitochondria. (B) Peaks have been discretized as spheres to ease the counting process. (C) Quantification of the percentage of peaks in each cellular compartment.

SVR of 1.6 and 2.8 respectively. Pericytes are in general flat cells with a fairly homogeneous morphology that are like sheets wrapped around the blood vessels (Fig. 8B) and interface with the astrocytic vascular endfeet (Fig. 6).

Astrocytes have highly variable morphology, and although their average SVR is similar to pericytes, the SVR of morphologically distinct astrocytic domains varies widely. We measured the contact surface area to volume ratio of astrocytic perivascular processes (Fig. 6) to be close to 1 while the smallest processes in the neuropil has been reported to have values up to 14 (Hama et al., 2004). Astrocytes clearly have a much higher surface area compared to neurons and therefore have a much larger membrane interface with the parenchyma around them. While all reconstructed astrocytes have a very simple morphological backbone with four primary processes (Fig. 5B), similar to neurons (Fig. 7), their full morphology (Fig. 5A) can include up to thousands of branches.

Interestingly, astrocytes 2 and 3 have three times more processes than astrocyte 1 and 4 (Fig. 5). Their proximity to each other makes it unlikely that such difference might arise from neuronal network

diversity, although we cannot rule this out. More probable reason for these differences is that at this stage of development (P14, age is crucial for synaptogenesis), some astrocytes not yet fully developed. This difference is also supported by astrocytes 2 and 3 having higher absolute volume and surface area (Fig. 4C). In contrast, the minimum and maximum width of cell seem unrelated with the branching of the cells.

The high branching order of an astrocyte is due to the large number of lamelliform processes stemming from its primary processes. In neurons, dendritic spines generate hundreds of spines (Fig. 7), similar to hundreds, or thousands of astrocytic lamelliform processes stemming from main processes. Dendritic spines are input stations for dendrites, and have a simpler morphology than astrocytic processes, because the surface area dedicated to the interaction with the volume in their proximity is mostly polarized towards the PSD. But even when we compare the branching order of a neuron in terms of number of spines to astrocytes there is a difference of a factor 10 (hundreds for neurons while up to thousands for astrocytes; Figs. 5 and 7). This suggests that the higher SVR in astrocytes is an indication of their capacity to interact

with multiple structures at once. The only known specialized astrocytic structure, the perivascular process (Fig. 6), indeed has a small SVR in spite of its relatively large interactive surface.

4.4. Mitochondria

We identified and reconstructed individual mitochondria from within each reconstructed cell (Fig. 10). It is a matter of general knowledge that mitochondria provide cells energy by transforming metabolites into ATP via oxidative phosphorylation using the Krebs cycle. However, under anoxia, cells can generate smaller amounts of ATP in glycolysis and pass to the resulting pyruvate to lactate instead. This is what happens to muscle cells during intense activity when the oxygen supply is not adequate (Cali et al., 2019). Also, tumor cells mainly rely on glycolysis even when oxygen is available using a mechanism called aerobic glycolysis or Warburg effect (Magistretti, 2014). In brain, neurons die shortly after oxygen deprivation, whereas astrocytes are able to survive solely on glycolysis, even for many years (Supplie et al., 2017). Not surprisingly, astrocytes are the site of aerobic glycolysis very similar to cancer cells (Magistretti and Allaman, 2018). The lactate that they produce through this pathway supports neurons in both their energetic and signaling functions as detailed in the astrocyte-neuron lactate shuttle (ANLS) model (Magistretti and Allaman, 2015, 2018).

The shape of mitochondria has recently been associated with cognitive impairments. During aging, presynaptic mitochondria acquire a “donut” shape that can be rescued with estrogen, and has been associated with decreased learning abilities (Hara et al., 2016). Dendritic mitochondria have been shown to acquire an elongated shape, which seems to indicate impaired fission, as seen in a genetic Alzheimer’s disease model (Zhang et al., 2016). Therefore, a simple assessment, in terms of global cell occupancy, and/or shape, might indicate differences in metabolic function between different cell types, although the present study is concerned with cells in physiological conditions. We quantified the percentage of mitochondrial occupancy against total cell volume, but could not observe any significant difference between cell types (Fig. 10E), although there seems to be a trend, similar to surface area to volume ratio (SVR) measurements, where astrocytes are more similar to pericytes, and neurons to microglia.

Distribution of mitochondria within individual neurons and microglia (examples in Fig. 10B–C) shows that, as a rule of thumb, they concentrate to main processes. Pericytes (Fig. 10C) that are flat cells lacking any visually distinct subdomain show no evident bias in mitochondrial distribution.

Interestingly, in astrocytes (Fig. 10A), mitochondria follow the main processes in a “GFAP-like” fashion, while a few, scattered mitochondria are present within smaller processes, with a width of at least 200 nm, roughly the size of a single tubule. This is in contrast with recent literature showing a widespread activity of mitochondria across most of the cell (Agarwal et al., 2017; Bindocci et al., 2017). This difference could be due to the early stage of development (P14) where the energy generation of mitochondria is still directed to internal rather than external use. At this stage, P14 neuronal networks are still forming and stabilizing, therefore the absence of mitochondria in astrocyte lamellar processes might correlate with a more important glycolysis within the neuropil controlled by individual astrocytes. This would necessarily result in an enhanced astrocytic L-Lactate production that would be locally shuttled to neuronal domains to sustain the structural maturation of neuronal processes, which is energetically expensive. Moreover, since, astrocytic lamelliform processes have a cross section of tenths of nanometers, where mitochondria cannot fit, ATP synthesis should necessarily pass through glycolysis, also taking into account that lamelliform processes are rich in glycogen (Cali et al., 2016).

The size of individual mitochondrial tubules might give an indication of their activity. The dynamics of fission and fusion are important indicators of a healthy mitochondria (Archer, 2013; Chen et al., 2005;

Suen et al., 2008), and impaired fission might be related to pathological conditions such as Alzheimer’s disease (Zhang et al., 2016). The average length of the mitochondria for all cells and cell types was longer in the processes compared to the soma, possibly indicating that the metabolic needs of the cells are highly compartmentalized. A higher average length in astrocytes than in neurons might suggest a higher glycolytic activity in glial cells compared to neurons (Supplie et al., 2017), although the measure is reversed in processes, where neurons shows a longer average length of mitochondria. This could be due to very long tubules present in the long proximal dendrites of neurons, in particular neuron 2 which has one 35 μm length mitochondrion. Such measurement differs from a recent report, where observations on individual mitochondria reconstructed in neurons imaged using expansion microscopy (Gao et al., 2019) reported a distribution of lengths ranging from 0.2 to 8 μm , which is similar to what we found among the 2nd and 98th percentile was ranging (0.2 and 10 μm), and to the range we observe in the soma (0.1–9.8 μm). The reasons for these differing results could equally well stem from different species or developmental stage of the samples or from some unknown physiological factor.

To further characterize the possible interaction of mitochondria with the environment within different cells, we performed a semi-quantitative analysis that is based on the GLAM paradigm (Agus et al., 2018a; Cali et al., 2017) where we considered mitochondria as a source of light, and counted the absorbing peaks on the membrane of each cell, all within a Virtual Reality (VR) head mounted display environment. Peaks were then plotted on the surfaces as spheres (Fig. 10F, bottom panels) and we counted manually how many were distributed in the different compartments. For neurons and microglia (grey and yellow bars, respectively), the highest concentrations of mitochondria were present on individual processes with neurons showing the vast majority of them in dendrites. Astrocytes (green bars) showed a variable distribution, with number 1 and 4 having less polarized peaks towards the perivascular processes, compared to number 2 and 3 that showed an opposite trend. Interestingly, these latter two cells are more branched (Fig. 5). Keeping the rapidly developing stage of the sample in mind, the correlation between the polarization of the perivascular distribution of the mitochondria and the branching level might suggest a difference in the maturity of the cells. In those cells, whose perivascular process are also larger in terms of surface area and volume indicating higher maturity (Fig. 6). Finally, pericytes did not show any particular preference between luminal and parenchymal portion of the brain, two of the studied cells (1 and 2) showing an opposite preference compared to the other two (3 and 4). Taken individually, pericytes 1 and 2 sit on a vascular bifurcation (Fig. 8A and B), compared to number 3 and 4 which are surrounding a straight segment; we could speculate that their energetic reserves need to be spent differently based on their location but this needs more observations to be relied on.

5. Conclusions

In this work, we were able for the first time to describe detailed 3D morphologies of neurons and glial cells using 3DEM. Technical advances in reconstructing complex astrocytic structures are finally opening them up to precise morphological analysis. In addition, we were able to place complete intracellular mitochondrial distributions to that morphology that allowed us to speculate on functional relevance of this distribution.

Within this framework, which is common to connectomics, one can envision a widespread study of all other brain cell types, whose morphological features are still poorly understood, but need to be investigated, to make sense of many physiological roles supposedly mediated by cells like astrocytes, that are still not completely understood.

6. Funding

This work was supported by the King Abdullah University of Science and Technology (KAUST) Office of Sponsored Research (OSR) under Award No. 3438 "KAUST-EPFL Alliance for Integrative Modeling of Brain Energy Metabolism".

Acknowledgements

We thank all the students and interns from the various KAUST programs, including VSRP, VS and KGSP, that participated to the segmentation of this dataset: Nicolas Gagnon, Fernanda Vargas, Jose Maria Martinez De Paz, Mohammed Jawhari, Dana Almedallah, Danielle Gaitor, Tajamul Hussain, Hajar AlReefi, Juamanh Alsawaf, Fatima Albazron, Bayan Khojah, Jumana Baghabra, Rana Alrabeh, and a very special thanks to Mohammed AlThunayan, a very talented student who passed away in his 20s. We also thank the KVL for the technical support, in particular Glendon Holst and Thomas Theussl. We thank Paola Bezzi (DNF, UNIL) for kindly providing brain sections for EM analysis, Graham Knott and Stephanie Rosset (BioEM, EPFL) for the technical support in the preparation of the sample for EM.

Appendix A. The Peer Review Overview and Supplementary data

The Peer Review Overview and Supplementary data associated with this article can be found in the online version, at doi: <https://doi.org/10.1016/j.pneurobio.2019.101696>.

References

- Abdollahzadeh, A., Belevich, I., Jokitalo, E., Tohka, J., Sierra, A., 2019. Automated 3D axonal morphometry of white matter. *Sci. Rep.* 9, 6084. <https://doi.org/10.1038/s41598-019-42648-2>.
- Agarwal, A., Wu, P.-H., Hughes, E.G., Fukaya, M., Tischfield, M.A., Langseth, A.J., Wirtz, D., Bergles, D.E., 2017. Transient opening of the mitochondrial permeability transition pore induces microdomain calcium transients in astrocyte processes. *Neuron* 93 <https://doi.org/10.1016/j.neuron.2016.12.034>. 587–605.e7.
- Agus, Marco, Boges, D., Gagnon, N., Magistretti, P.J., Hadwiger, M., Cali, C., 2018a. GLAM: glycogen-derived lactate absorption map for visual analysis of dense and sparse surface reconstructions of rodent brain structures on desktop systems and virtual environments. Dryad Digital Repository. <https://doi.org/10.5061/dryad.808k4r0>.
- Agus, Marco, Boges, D., Gagnon, N., Magistretti, P.J., Hadwiger, M., Cali, C., 2018b. GLAM: glycogen-derived lactate absorption map for visual analysis of dense and sparse surface reconstructions of rodent brain structures on desktop systems and virtual environments. *Comput. Graph.* 74, 85–98. <https://doi.org/10.1016/j.cag.2018.04.007>.
- Agus, M., Cali, C., Morales, A.T., Lehvälaiho, H.O., Magistretti, P.J., Gobetti, E., Hadwiger, M., 2018c. Hyperquadrics for shape analysis of 3D nanoscale reconstructions of brain cell nuclear envelopes. In: Proceedings of the Smart Tools and Apps for Graphics-Eurographics Italian Chapter Conference. The Eurographics Association. pp. 115–122. <https://doi.org/10.2312/stag.20181304>.
- Agus, M., Cali, C., Al-Awami, A.K., Gobetti, E., Magistretti, P.J., Hadwiger, M., 2019a. Interactive volumetric visual analysis of glycogen-derived energy absorption in nanometric brain structures. *Comput. Graph. Forum* 38 (3), 427–439. <https://doi.org/10.1111/cgf.13700>.
- Agus, M., Veloz Castillo, M., Garnica Molina, J.F., Gobetti, E., Lehvälaiho, H., Morales Tapia, A., Magistretti, P.J., Hadwiger, M., Cali, C., 2019b. Shape analysis of 3D nanoscale reconstructions of brain cell nuclear envelopes by implicit and explicit parametric representations. *Comput. Graph.: X 1*, 100004. <https://doi.org/10.1016/j.cagx.2019.100004>.
- Archer, S.L., 2013. Mitochondrial dynamics—mitochondrial fission and fusion in human diseases. *N. Engl. J. Med.* 369, 2236–2251. <https://doi.org/10.1056/NEJMr1215233>.
- Bindocci, E., Savtchouk, I., Liaudet, N., Becker, D., Carriero, G., Volterra, A., 2017. Three-dimensional Ca(2+) imaging advances understanding of astrocyte biology. *Science* 356. <https://doi.org/10.1126/science.aai8185>.
- Bisht, K., Sharma, K., Lacoste, B., Tremblay, M.-È., 2016. Dark microglia: why are they dark? *Commun. Integr. Biol.* 9. <https://doi.org/10.1080/19420889.2016.1230575>.
- Boulay, A.-C., Saubaméa, B., Adam, N., Chasseigneaux, S., Mazaré, N., Gilbert, A., Bahin, M., Bastianelli, L., Blugeon, C., Perrin, S., Pouch, J., Ducos, B., Le Crom, S., Genovesio, A., Chrétien, F., Declèves, X., Laplanche, J.-L., Cohen-Salmon, M., 2017. Translation in astrocyte distal processes sets molecular heterogeneity at the gliovascular interface. *Cell Discov.* 3, 17005. <https://doi.org/10.1038/celldisc.2017.5>.
- Bourne, J.N., Harris, K.M., 2011. Coordination of size and number of excitatory and inhibitory synapses results in a balanced structural plasticity along mature hippocampal CA1 dendrites during LTP. *Hippocampus* 21, 354–373. <https://doi.org/10.1002/hipo.20768>.
- Butt, A., Kiff, J., Hubbard, P., Berry, M., 2002. Synaptocytes: new functions for novel NG2 expressing glia. *J. Neurocytol.* 551–565.
- Cali, C., 2017. Astroglial anatomy in the times of connectomics. *J. Transl. Neurosci.* 2, 31–40. <https://doi.org/10.3868/j.issn.2096-0689.2017.04.004>.
- Cali, C., Agus, M., Gagnon, N., Hadwiger, M., Magistretti, P.J., 2017. Visual analysis of glycogen derived lactate absorption in dense and sparse surface reconstructions of rodent brain structures. Eurographics Italian Chapter Conference 2017 Sep 11 31–38. <https://doi.org/10.2312/stag.20171224>.
- Cali, C., Baghabra, J., Boges, D.J., Holst, G.R., Kreshuk, A., Hamprecht, F.A., Srinivasan, M., Lehvälaiho, H., Magistretti, P.J., 2016. Three-dimensional immersive virtual reality for studying cellular compartments in 3D models from EM preparations of neural tissues. *J. Comp. Neurol.* 524, 23–38. <https://doi.org/10.1002/cne.23852>.
- Cali, C., Tauffenberger, A., Magistretti, P., 2019. The strategic location of Glycogen and lactate: from body energy reserve to brain plasticity. *Front. Cell. Neurosci.* 13. <https://doi.org/10.3389/fncel.2019.00082>.
- Cali, C., Wawrzyniak, M., Becker, C., Maco, B., Cantoni, M., Jorstad, A., Nigro, B., Grillo, F., Paola, V.D., Fua, P., Knott, G.W., 2018. The effects of aging on neuropil structure in mouse somatosensory cortex—a 3D electron microscopy analysis of layer 1. *PLoS One* 13, e0198131. <https://doi.org/10.1371/journal.pone.0198131>.
- Cao, T., Zhou, X., Zheng, X., Cui, Y., Tsien, J.Z., Li, C., Wang, H., 2018. Histone deacetylase inhibitor alleviates the neurodegenerative phenotypes and histone dysregulation in presenilin-deficient mice. *Front. Aging Neurosci.* 10, 137. <https://doi.org/10.3389/fnagi.2018.00137>.
- Chelini, G., Pantazopoulos, H., Durning, P., Berretta, S., 2018. The tetrapartite synapse: a key concept in the pathophysiology of schizophrenia. *Eur. Psychiatry* 50, 60–69. <https://doi.org/10.1016/j.eurpsy.2018.02.003>.
- Chen, H., Chomyn, A., Chan, D.C., 2005. Disruption of fusion results in mitochondrial heterogeneity and dysfunction. *J. Biol. Chem.* 280, 26185–26192. <https://doi.org/10.1074/jbc.M503062200>.
- Coggan, J.S., Cali, C., Keller, D., Agus, M., Boges, D., Abdellah, M., Kare, K., Lehvälaiho, H.O., Eilemann, S., Jolivet, R.B., Hadwiger, M., Markram, H., Schürmann, F., Magistretti, P.J., 2018. A process for digitizing and simulating biologically realistic oligocellular networks demonstrated for the neuro-glio-vascular ensemble. *Front. Neurosci.* 12. <https://doi.org/10.3389/fnins.2018.00664>.
- Deerinck, T.J., Bushong, E.A., Lev-Ram, V., Shu, X., Tsien, R.Y., Ellisman, M.H., 2010. Enhancing serial block-face scanning electron microscopy to enable high resolution 3-D nanohistology of cells and tissues. *Microsc. Microanal.* 16, 1138–1139. <https://doi.org/10.1017/S1431927610055170>.
- Deerinck, T.J., Shone, T.M., Bushong, E.A., Ramachandra, R., Peltier, S.T., Ellisman, M.H., 2018. High-performance serial block-face SEM of nonconductive biological samples enabled by focal gas injection-based charge compensation. *J. Microsc.* 270, 142–149. <https://doi.org/10.1111/jmi.12667>.
- Della Santina, L., Kuo, S.P., Yoshimatsu, T., Okawa, H., Suzuki, S.C., Hoon, M., Tsuboyama, K., Rieke, F., Wong, R.O.L., 2016. Glutamatergic monopolar interneurons provide a novel pathway of excitation in the mouse retina. *Curr. Biol.* 26, 2070–2077. <https://doi.org/10.1016/j.cub.2016.06.016>.
- Gao, R., Asano, S.M., Upadhyayula, S., Pisarev, I., Milkie, D.E., Liu, T.-L., Singh, V., Graves, A., Huynh, G.H., Zhao, Y., Bogovic, J., Colonell, J., Ott, C.M., Zugasas, C., Tappan, S., Rodriguez, A., Mosaliganti, K.R., Sheu, S.-H., Pasolli, H.A., Pang, S., Xu, C.S., Megason, S.G., Hess, H., Lippincott-Schwartz, J., Hantman, A., Rubin, G.M., Kirchhausen, T., Saalfeld, S., Aso, Y., Boyden, E.S., Betzig, E., 2019. Cortical column and whole-brain imaging with molecular contrast and nanoscale resolution. *Science* 363 <https://doi.org/10.1126/science.aau8302>. eaau8302.
- Gillooly, J.F., Hein, A., Damiani, R., 2015. Nuclear DNA content varies with cell size across human cell types. *Cold Spring Harb. Perspect. Biol.* 7. <https://doi.org/10.1101/cshperspect.a019091>.
- Graydon, C.W., Lieberman, E.E., Rho, N., Briggman, K.L., Singer, J.H., Diamond, J.S., 2018. Synaptic transfer between rod and cone pathways mediated by AII amacrine cells in the mouse retina. *Curr. Biol.* 28 <https://doi.org/10.1016/j.cub.2018.06.063>. 2739–2751.e3.
- Hama, K., Arii, T., Katayama, E., Marton, M., Ellisman, M.H., 2004. Tri-dimensional morphometric analysis of astrocytic processes with high voltage electron microscopy of thick Golgi preparations. *J. Neurocytol.* 33, 277–285. <https://doi.org/10.1023/B:NEUR.0000044189.08240.a2>.
- Hara, Y., Yuk, F., Puri, R., Janssen, W.G.M., Rapp, P.R., Morrison, J.H., 2016. Estrogen restores multisynaptic boutons in the dorsolateral prefrontal cortex while promoting working memory in aged rhesus monkeys. *J. Neurosci.* 36, 901–910. <https://doi.org/10.1523/JNEUROSCI.3480-13.2016>.
- Harris, K.M., Spacek, J., Bell, M.E., Parker, P.H., Lindsey, L.F., Baden, A.D., Vogelstein, J.T., Burns, R., 2015. A resource from 3D electron microscopy of hippocampal neuropil for user training and tool development. *Nat. Sci. Data* 2, 150046. <https://doi.org/10.1038/sdata.2015.46>.
- Herculano-Houzel, S., 2014. The glia/neuron ratio: how it varies uniformly across brain structures and species and what that means for brain physiology and evolution: the glia/neuron ratio. *Glia* 62, 1377–1391. <https://doi.org/10.1002/glia.22683>.
- Holst, G., Berg, S., Kare, K., Magistretti, P., Cali, C., 2016. Adding large EM stack support. IEEE 1–7. <https://doi.org/10.1109/KACSTIT.2016.7756066>.
- Hughes, L., Borrett, S., Towers, K., Starborg, T., Vaughan, S., 2017. Patterns of organelle ontogeny through a cell cycle revealed by whole-cell reconstructions using 3D electron microscopy. *J. Cell. Sci.* 130, 637–647. <https://doi.org/10.1242/jcs.198887>.
- Januszewski, M., Kornfeld, J., Li, P.H., Pope, A., Blakely, T., Lindsey, L., Maitin-Shepard, J., Tyka, M., Denk, W., Jain, V., 2018. High-precision automated reconstruction of neurons with flood-filling networks. *Nat. Methods* 1. <https://doi.org/10.1038/s41592-018-0049-4>.

- Jorstad, A., Nigro, B., Cali, C., Wawrzyniak, M., Fua, P., Knott, G., 2015. NeuroMorph: a toolset for the morphometric analysis and visualization of 3D models derived from electron microscopy image stacks. *Neuroinformatics* 13, 83–92. <https://doi.org/10.1007/s12021-014-9242-5>.
- Kasthuri, N., Hayworth, K.J., Berger, D.R., Schalek, R.L., Conchello, J.A., Knowles-Barley, S., Lee, D., Vázquez-Reina, A., Kaynig, V., Jones, T.R., Roberts, M., Morgan, J.L., Tapia, J.C., Seung, H.S., Roncal, W.G., Vogelstein, J.T., Burns, R., Sussman, D.L., Priebe, C.E., Pfister, H., Lichtman, J.W., 2015. Saturated reconstruction of a volume of neocortex. *Cell* 162, 648–661. <https://doi.org/10.1016/j.cell.2015.06.054>.
- Knott, G., Genoud, C., 2013. Is EM dead? *J. Cell. Sci.* 126, 4545–4552. <https://doi.org/10.1242/jcs.124123>.
- Korogod, N., Petersen, C.C.H., Knott, G.W., 2015. Ultrastructural analysis of adult mouse neocortex comparing aldehyde perfusion with cryo fixation. *Elife* 4. <https://doi.org/10.7554/eLife.05793>.
- Kreshuk, A., Walecki, R., Koethe, U., Gierthmuehlen, M., Plachta, D., Genoud, C., Haastert-Talini, K., Hamprecht, F.A., 2015. Automated tracing of myelinated axons and detection of the nodes of Ranvier in serial images of peripheral nerves. *J. Microsc.* 259, 143–154. <https://doi.org/10.1111/jmi.12266>.
- Magistretti, P.J., 2014. Synaptic plasticity and the Warburg effect. *Cell Metab.* 19, 4–5. <https://doi.org/10.1016/j.cmet.2013.12.012>.
- Magistretti, P.J., Allaman, I., 2018. Lactate in the brain: from metabolic end-product to signalling molecule. *Nat. Rev. Neurosci.* 19, 235–249. <https://doi.org/10.1038/nrn.2018.19>.
- Magistretti, P.J., Allaman, I., 2015. A cellular perspective on brain energy metabolism and functional imaging. *Neuron* 86, 883–901. <https://doi.org/10.1016/j.neuron.2015.03.035>.
- Mathiisen, T.M., Lehre, K.P., Danbolt, N.C., Ottersen, O.P., 2010. The perivascular astroglial sheath provides a complete covering of the brain microvessels: an electron microscopic 3D reconstruction. *Glia* 58, 1094–1103. <https://doi.org/10.1002/glia.20990>.
- Maze, I., Noh, K.-M., Allis, C.D., 2013. Histone regulation in the CNS: basic principles of epigenetic plasticity. *Neuropsychopharmacology* 38, 3–22. <https://doi.org/10.1038/npp.2012.124>.
- Mohammed, H., Al-Awami, A.K., Beyer, J., Cali, C., Magistretti, P., Pfister, H., Hadwiger, M., 2017. Abstractocyte: a visual tool for exploring nanoscale astroglial cells. *IEEE Trans. Vis. Comput. Graph.* <https://doi.org/10.1109/TVCG.2017.2744278>.
- Morgan, J.L., Berger, D.R., Wetzal, A.W., Lichtman, J.W., 2016. The fuzzy logic of network connectivity in mouse visual thalamus. *Cell* 165, 192–206. <https://doi.org/10.1016/j.cell.2016.02.033>.
- Murakami, T., Murakami, T., Mahmut, N., Hitomi, S., Ohtsuka, A., 1997. Dark and light neurons in the human brain, with special reference to their reactions to Golgi's silver nitrate, luxol fast blue MBS and azocarmine G. *Arch. Histol. Cytol.* 60, 265–274.
- Navarro, P.P., Genoud, C., Castaño-Díez, D., Graff-Meyer, A., Lewis, A.J., de Gier, Y., Lauer, M.E., Britschgi, M., Bohrmann, B., Frank, S., Hench, J., Schweighauser, G., Rozemuller, A.J.M., van de Berg, W.D.J., Stahlberg, H., Shahmoradian, S.H., 2018. Cerebral Corpora amylacea are dense membranous labyrinths containing structurally preserved cell organelles. *Sci. Rep.* 8, 18046. <https://doi.org/10.1038/s41598-018-36223-4>.
- Nicholson, C., Hrabětová, S., 2017. Brain extracellular space: the final frontier of neuroscience. *Biophys. J.* 113, 2133–2142. <https://doi.org/10.1016/j.bpj.2017.06.052>.
- Nimmerjahn, A., Kirchhoff, F., Helmchen, F., 2005. Resting microglial cells are highly dynamic surveillants of brain parenchyma in vivo. *Science* 308, 1314–1318. <https://doi.org/10.1126/science.1110647>.
- Penney, J., Tsai, L.-H., 2014. Histone deacetylases in memory and cognition. *Sci. Signal.* 7 <https://doi.org/10.1126/scisignal.aaa0069>. re12.
- Puhka, M., Joensuu, M., Vihinen, H., Belevich, I., Jokitalo, E., 2012. Progressive sheet-to-tubule transformation is a general mechanism for endoplasmic reticulum partitioning in dividing mammalian cells. *Mol. Biol. Cell* 23, 2424–2432. <https://doi.org/10.1091/mbc.E10-12-0950>.
- Rat Genome Sequencing Project Consortium, 2004. Genome sequence of the Brown Norway rat yields insights into mammalian evolution. *Nature* 428, 493–521. <https://doi.org/10.1038/nature02426>.
- Santuy, A., Rodriguez, J.R., DeFelipe, J., Merchan-Perez, A., 2018. Volume electron microscopy of the distribution of synapses in the neuropil of the juvenile rat somatosensory cortex. *Brain Struct. Funct.* 223, 77–90. <https://doi.org/10.1007/s00429-017-1470-7>.
- Savage, J.C., Picard, K., González-Ibáñez, F., Tremblay, M.-È., 2018. A brief history of microglial ultrastructure: distinctive features, phenotypes, and functions discovered over the past 60 years by electron microscopy. *Front. Immunol.* 9, 803. <https://doi.org/10.3389/fimmu.2018.00803>.
- Shepherd, G.M., Harris, K.M., 1998. Three-dimensional structure and composition of CA3-&CA1 axons in rat hippocampal slices: implications for presynaptic connectivity and compartmentalization. *J. Neurosci.* 18, 8300–8310.
- Shu, G., Kramár, E.A., López, A.J., Huynh, G., Wood, M.A., Kwapis, J.L., 2018. Deleting HDAC3 rescues long-term memory impairments induced by disruption of the neuron-specific chromatin remodeling subunit BAF53b. *Learn. Mem.* 25, 109–114. <https://doi.org/10.1101/lm.046920.117>.
- Stuart, G., Spruston, N., Häusser, M., 2016. *Dendrites*, third edition. Oxford University Press, Oxford, New York.
- Suen, D.-F., Norris, K.L., Youle, R.J., 2008. Mitochondrial dynamics and apoptosis. *Genes Dev.* 22, 1577–1590. <https://doi.org/10.1101/gad.1658508>.
- Supplie, L.M., Dürking, T., Campbell, G., Diaz, F., Moraes, C.T., Götz, M., Hamprecht, B., Boretius, S., Mahad, D., Nave, K.-A., 2017. Respiration-deficient astrocytes survive as glycolytic cells in vivo. *J. Neurosci.* 37, 4231–4242. <https://doi.org/10.1523/JNEUROSCI.0756-16.2017>.
- Thevenaz, P., Ruttimann, U.E., Unser, M., 1998. A pyramid approach to subpixel registration based on intensity. *IEEE Trans. Image Process.* 7, 27–41. <https://doi.org/10.1109/83.650848>.
- Thion, M.S., Garel, S., 2018. Microglia under the spotlight: activity and complement-dependent engulfment of synapses. *Trends Neurosci.* 41, 332–334. <https://doi.org/10.1016/j.tins.2018.03.017>.
- Tomassy, G.S., Berger, D.R., Chen, H.-H., Kasthuri, N., Hayworth, K.J., Vercelli, A., Seung, H.S., Lichtman, J.W., Arlotta, P., 2014. Distinct profiles of myelin distribution along single axons of pyramidal neurons in the neocortex. *Science* 344, 319–324. <https://doi.org/10.1126/science.1249766>.
- von Bartheld, C.S., Bahnney, J., Herculano-Houzel, S., 2016. The search for true numbers of neurons and glial cells in the human brain: a review of 150 years of cell counting: quantifying neurons and glia in human brain. *J. Comp. Neurol.* 524, 3865–3895. <https://doi.org/10.1002/cne.24040>.
- Walsh, M.E., Bhattacharya, A., Sataranatarajan, K., Qaisar, R., Sloane, L., Rahman, M.M., Kinter, M., Van Remmen, H., 2015. The histone deacetylase inhibitor butyrate improves metabolism and reduces muscle atrophy during aging. *Aging Cell* 14, 957–970. <https://doi.org/10.1111/acer.12387>.
- Witcher, M.R., Kirov, S.A., Harris, K.M., 2007. Plasticity of perisynaptic astroglia during synaptogenesis in the mature rat hippocampus. *Glia* 55, 13–23. <https://doi.org/10.1002/glia.20415>.
- Witcher, M.R., Park, Y.D., Lee, M.R., Sharma, S., Harris, K.M., Kirov, S.A., 2010. Three-dimensional relationships between perisynaptic astroglia and human hippocampal synapses. *Glia* 58, 572–587. <https://doi.org/10.1002/glia.20946>.
- Wu, Y., Whiteus, C., Xu, C.S., Hayworth, K.J., Weinberg, R.J., Hess, H.F., Camilli, P.D., 2017. Contacts between the endoplasmic reticulum and other membranes in neurons. *PNAS* 114, E4859–E4867. <https://doi.org/10.1073/pnas.1701078114>.
- Zhang, L., Trushin, S., Christensen, T.A., Bachmeier, B.V., Gateno, B., Schroeder, A., Yao, J., Itoh, K., Sesaki, H., Poon, W.W., Gyls, K.H., Patterson, E.R., Parisi, J.E., Diaz Brinton, R., Salisbury, J.L., Trushina, E., 2016. Altered brain energetics induces mitochondrial fission arrest in Alzheimer's disease. *Sci. Rep.* 6, 18725. <https://doi.org/10.1038/srep18725>.
- Zheng, Z., Lauritzen, J.S., Perlman, E., Robinson, C.G., Nichols, M., Milkie, D., Torrens, O., Price, J., Fisher, C.B., Sharifi, N., Calle-Schuler, S.A., Kmecova, L., Ali, I.J., Karsh, B., Trautman, E.T., Bogovic, J.A., Hanslovsky, P., Jefferis, G.S.X.E., Kazhdan, M., Khairy, K., Saalfeld, S., Fetter, R.D., Bock, D.D., 2018. A complete electron microscopy volume of the brain of adult *Drosophila melanogaster*. *Cell* 174 <https://doi.org/10.1016/j.cell.2018.06.019>. 730–743.e22.